universität wien

MASTERARBEIT

Titel der Masterarbeit

„Investigation of the ternary phase diagram Au-Ni-Si“

verfasst von

Matthias Stacher BSc.

angestrebter akademischer Grad

Master of Science (MSc)

Wien, 2014

Studienkennzahl lt. Studienblatt:	A 066 862
Studienrichtung lt. Studienblatt:	Masterstudium Chemie
Betreut von:	ao. Univ.-Prof. Mag. Dr. Klaus Richter

Matthias Stacher, Department of Inorganic Chemistry (Materials Chemistry), University of Vienna, Währinger Str. 42, 1090 Wien, Austria

Preface

This work was performed from October 2013 to June 2014 in the working group of ao. Univ.-Prof. Mag. Dr. Klaus Richter at the Department of Inorganic Chemistry (Materials Chemistry).
I want to thank all the entire group of the institute for all the support they gave me and I enjoyed every day working with my friendly, competent and ambitious colleagues.
Special thanks go to Prof. Richter who gave me such an interesting master thesis and guided me through the entire work, especially if I lost my way on solving a problem.
I wish to thank ao.Univ.Prof. Herta Effenberger for her great work on analysing the crystal structures and Dr. Puchegger Stephan for his support on SEM/EPMA-measurements.

Table of content

Preface 2

Table of content 3

1 Introduction / Purpose 5

2 Theoretical background 6

2.1 Phase diagram [14-17] 6

2.2 Methods 10
2.2.1 Light optical microscopy (LOM) [15, 16] 10
2.2.2 Scanning electron microscopy (SEM) & electron probe microanalysis (EPMA) [22, 23] 12
2.2.3 Powder X-ray diffraction (powder-XRD) [15, 16, 24-26] 13
2.2.4 Single crystal X-ray diffraction [15, 16, 24, 26, 28] 15
2.2.5 Differential thermal analysis (DTA) [15, 16, 29] 17

3 Literature 19

3.1 Au-Si 19

3.2 Au-Ni 21

3.3 Ni-Si 22

3.4 Au-Ni-Si 24

4 Experimental 25

4.1 Sample preparation 25

4.2 Sample compositions 27

4.3 Experimental Procedures, Sample Analysis 29
4.3.1 Light optical microscopy (LOM) 29
4.3.2 Scanning electron microscopy 30
4.3.3 Powder X-ray diffraction (powder-XRD) 30
4.3.4 Single crystal X-ray diffraction 31
4.3.5 Differential thermal analysis (DTA) 32

5 Results and discussion 33

5.1 Isothermal sections 33
5.1.1 Isothermal section at 320°C 33
5.1.2 Isothermal section at 500°C 36
5.1.3 Metastable phase $Au_{17}Si_3$ 39
5.1.4 Isothermal section at 700°C 40

Table of content

5.2 The τ_1-Phase $Au_2Ni_4Si_7$ 44
5.2.1 Results of structure determination 46
5.2.2 Comparison τ_1 – $NiSi_2$ 48

5.3 The τ_2-Phase $AuNi_3Si_6$ 50
5.3.1 Results of structure determination 51
5.3.2 Comparison τ_2 – $NiSi_2$ 52

5.4 Scheil diagram (reaction scheme) 54

5.5 Isopleths 57
5.5.1 Isopleth 10 at.% Au 58
5.5.2 Isopleth 15 at.% Ni 59
5.5.3 Isopleth 30 at.% Ni 60
5.5.4 Isopleth 60 at.% Ni 61

5.6 Liquidus surface projection 62

5.7 Wetting experiments 63

6 Abstract 66

7 Zusammenfassung 67

8 References 68

9 Appendices 70

9.1 List of figures 70

9.2 List of tables 71

9.3 Curriculum Vitae 72

1 Introduction / Purpose

In many applications alloys are used, where their properties are superior to those of the pure component elements for a given application. To understand processes, phases and reactions of an alloy, the knowledge about the phase diagram is necessary [1]. A huge number of possible ternary phase diagrams exist and relatively few are described by now [2]. As information about the ternary system Au-Ni-Si is practically non-existent, this work explores the ternary phase diagram of gold, nickel and silicon.

Au-Si alloys may become attractive for joining applications, because of their low melting point. During joining, the Au-Si alloy can be in contact with metallization layers like Au, Cu, Ni, Cr or Ti, with Si (SiO2) wafers or with ceramics like SiC. Therefore, a fundamental knowledge of the wetting behavior and of the interface reactions with these substrates is required. In the past the wetting properties of Au-Si alloys on Si [3], SiO2 [4] and SiC [5-7] were studied. Up to now, no results concerning the wetting behavior or related interface reactions of Au-Si alloys on Ni substrates are available.

The knowledge of the properties of metal-semiconductor eutectic alloys like Au82Si18, and of their reactions with further elements like Ni is also very important for novel micro- and nano- electro mechanical systems (MEMS, NEMS), e.g.in high temperature Schottky diodes [8-10].

Furthermore the eutectic Au-Si alloy was the first ever discovered metallic glass [11], and gold-based metallic glasses exhibit desired mechanical properties for jewelry applications [12, 13].

To have a handle on all this mentioned applications, the knowledge about the ternary system Au-Ni-Si plays a major role. To get a full overview about this system, a reaction scheme (Scheil diagram), 3 isothermal sections (320, 500, 700℃), vertical sections (isopleths) and liquidus surface projections was constructed.

Finally, wetting experiments of the Au-Si eutectic composition on a nickel plate will be performed.

2 Theoretical background

2.1 Phase diagram [14-17]

A phase diagram is a fundamental chart used in materials chemistry, metallurgy, crystallography and other branches of materials science and gives information about a system consisting of one or more components. It is the graphical representation of the state of a system in thermodynamic equilibrium as a function of temperature, pressure and composition. At designated temperature and composition, it is possible to determine which phases will be formed, and in what quantities.

A single-component phase diagram can be simply a one- or two-dimensional plot showing the phase change in the substance as temperature and/or pressure change. Most diagrams are two-or three-dimensional plots describing the phase relationships in systems made up of two or more components, and these usually contain fields consisting of mixed-phase fields, as well as single-phase fields.

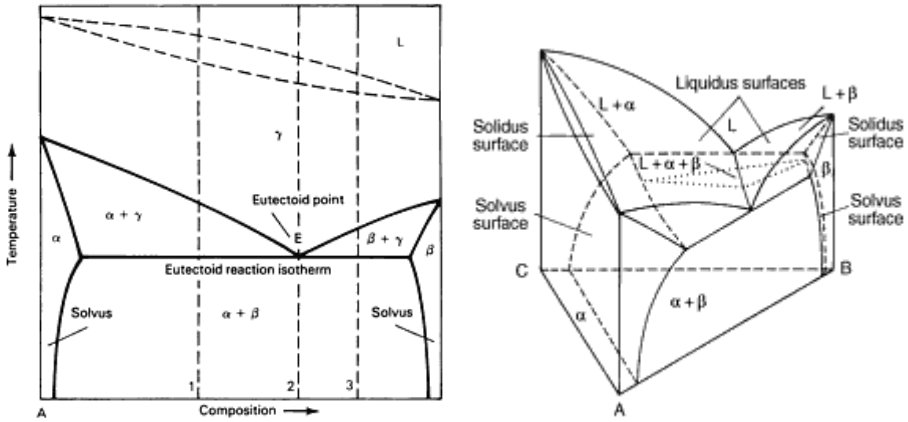

Figure 1: Binary and ternary phase diagram plots (schematic) [1, 18]

If a system is bordered by two components, the system is called a binary system. Usually the phase diagram is expressed by a two-dimensional plot of temperature and composition.

When a third component is added to a binary system, illustrating equilibrium conditions in two dimensions becomes more complicated. One option is to add a third composition dimension to the base, forming a 3-D-diagram having binary diagrams as its vertical sides (see Figure 1).

Illustrating the diagram for a ternary system is a challenge and is often represented with a series of two-dimensional horizontal sections (T=const.) and vertical sections

(isopleths, the fraction of one component or the ratio between two components is fixed).

Another two-dimensional representation is the liquidus surface projections, which is not isothermal. Therefore, isothermal contour lines are used to indicate the shape of the liquidus surface (see Figure 2). In addition to contour lines, views often show lines indicating the temperature troughs formed at the intersections of two surfaces. Arrowheads are often added to these lines to indicate the direction of decreasing temperature in the trough.

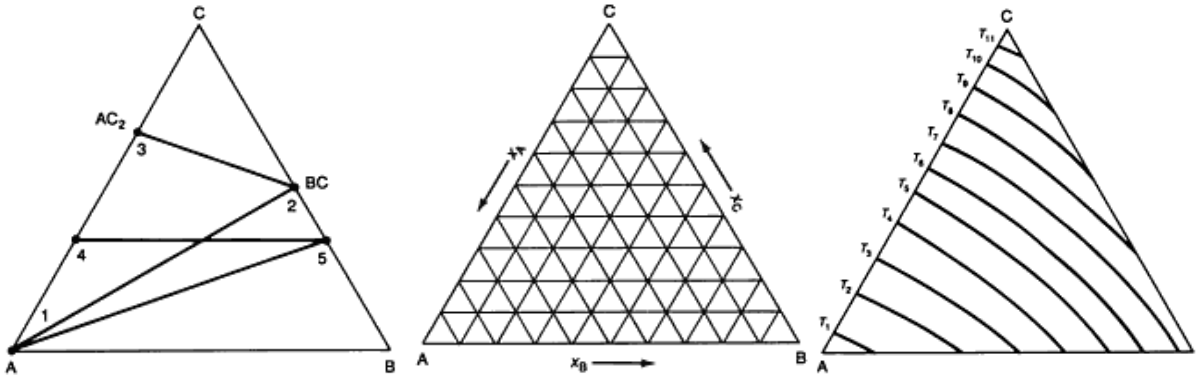

Figure 2: Projection of vertical sections, isothermal section and schematic liquidus surface view [1]

Phase diagrams to be used by scientists are usually plotted in atomic percentage (or mole fraction), while those to be used by engineers are usually plotted in weight percentage.

There are several rules for constructing/reading a phase diagram; three important are mentioned below:

The **Gibbs phase rule** applies to all states of matter (solid, liquid, and gaseous):

F = C - P + 2

But when the pressure is kept constant, the rule reduces to:

F = C - P + 1,

where F is the degree of freedom, C is the number of components, and P is the number of stable phases in the system.

The **Lever Rule**: A tie line is an imaginary horizontal line drawn in a two-phase field connecting two points that represent two coexisting phases in equilibrium at the temperature indicated by the line. Tie lines can be used to determine the fractional amounts n_α and n_β of the phases in equilibrium by employing the lever rule:

$$n_\alpha * l_\alpha = n_\beta * l_\beta$$

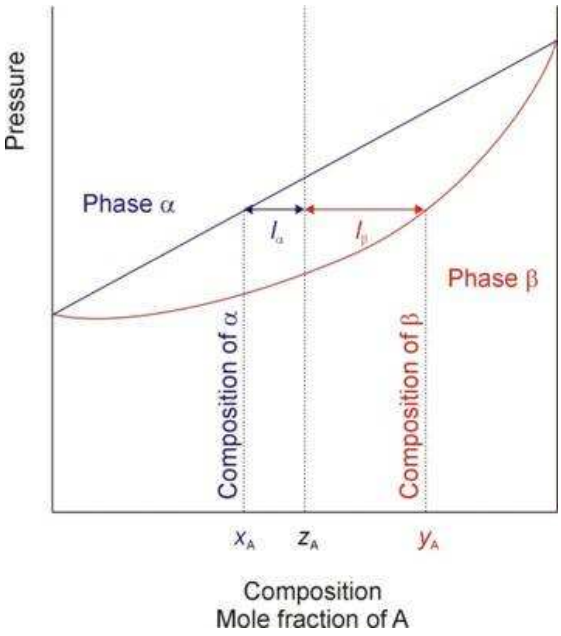

Figure 3: Binary phase diagram, lever rule [19]

Another rule is the **rule after Landau & Palatnik**, which describes the dimension of the borders between different phase fields:

$$D^+ + D^- = r - b$$

where D^+ and D^- represents the number of phases gained (D^+) and lost (D^-) during transition from one phase field to an other phase. Value r means the dimension of the phase diagram and the dimension of boundary between two neighbouring phase fields is represented by b (point=0, line=1).

In a binary system invariant reactions can occur in two different types: peritectic and eutectic type. In a ternary system there are following 3 different types of invariant reactions:

Eutectic reaction type: One phase decomposes on cooling into 3 new phases (see Figure 4).

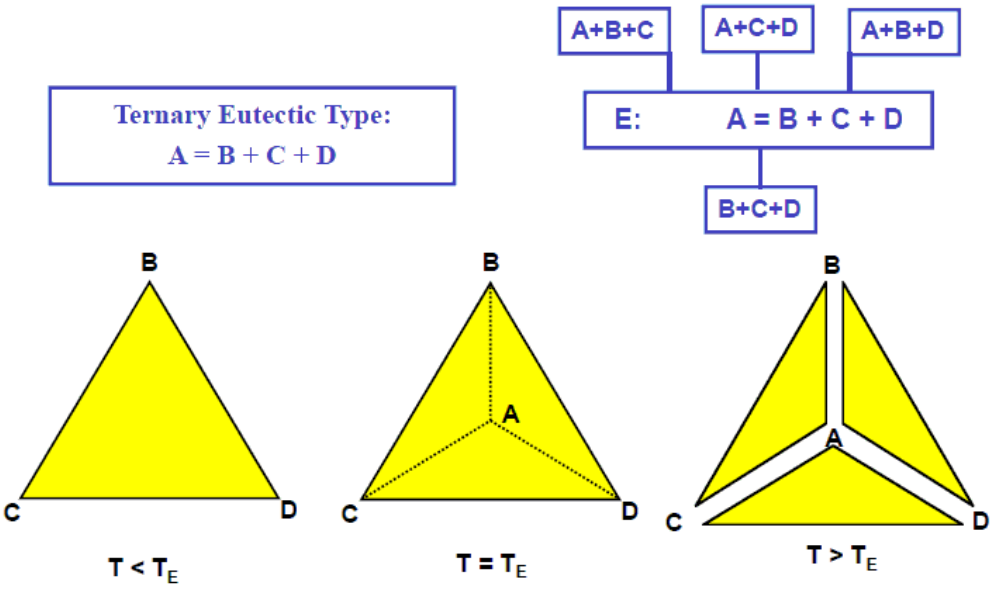

Figure 4: Ternary invariant reaction: ternary eutectic [15]

Peritectic reaction type: A mixture of 3 phases form into one new phase on cooling (see Figure 5).

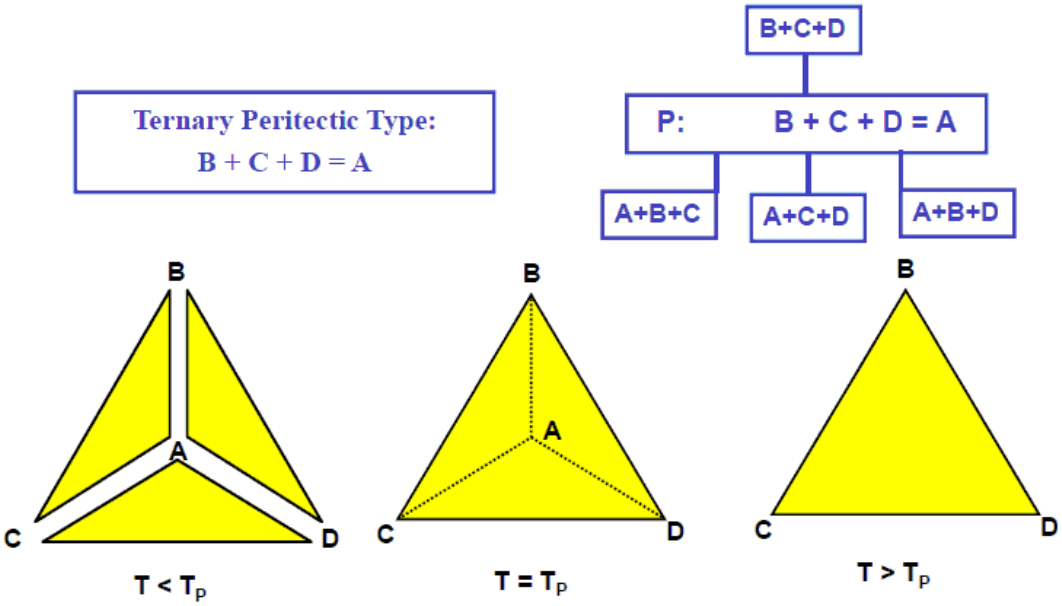

Figure 5: Ternary invariant reaction: ternary peritectic [15]

Transition reaction type: The phase boundary between two neighbouring 3-phase-field is changed (see Figure 6)

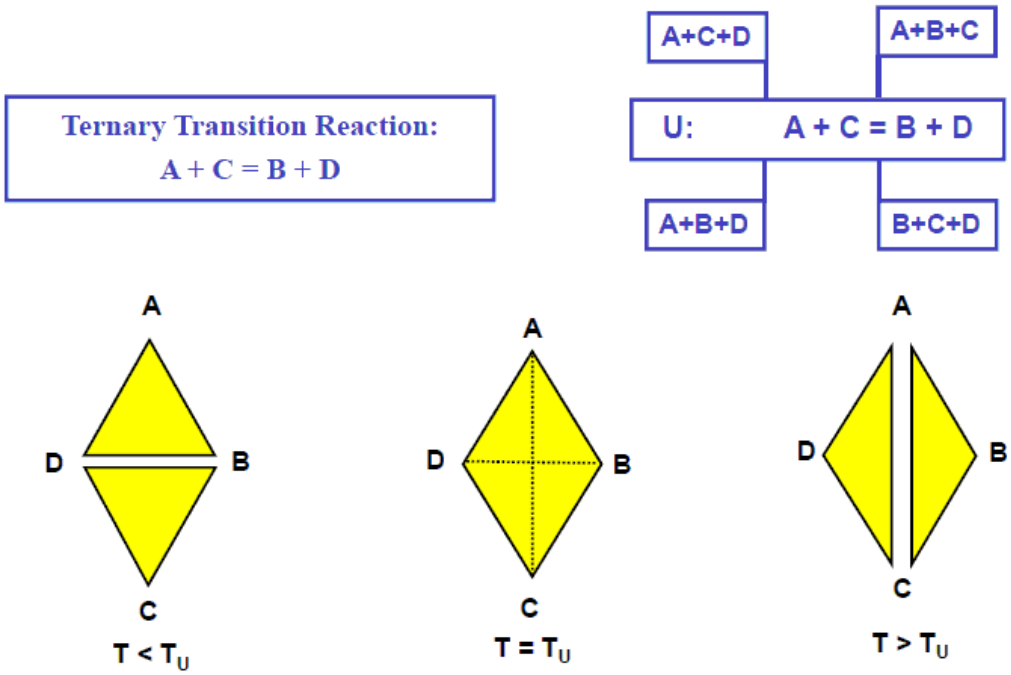

Figure 6: Ternary invariant reaction: ternary transition [15]

2.2 Methods

2.2.1 Light optical microscopy (LOM) [15, 16]

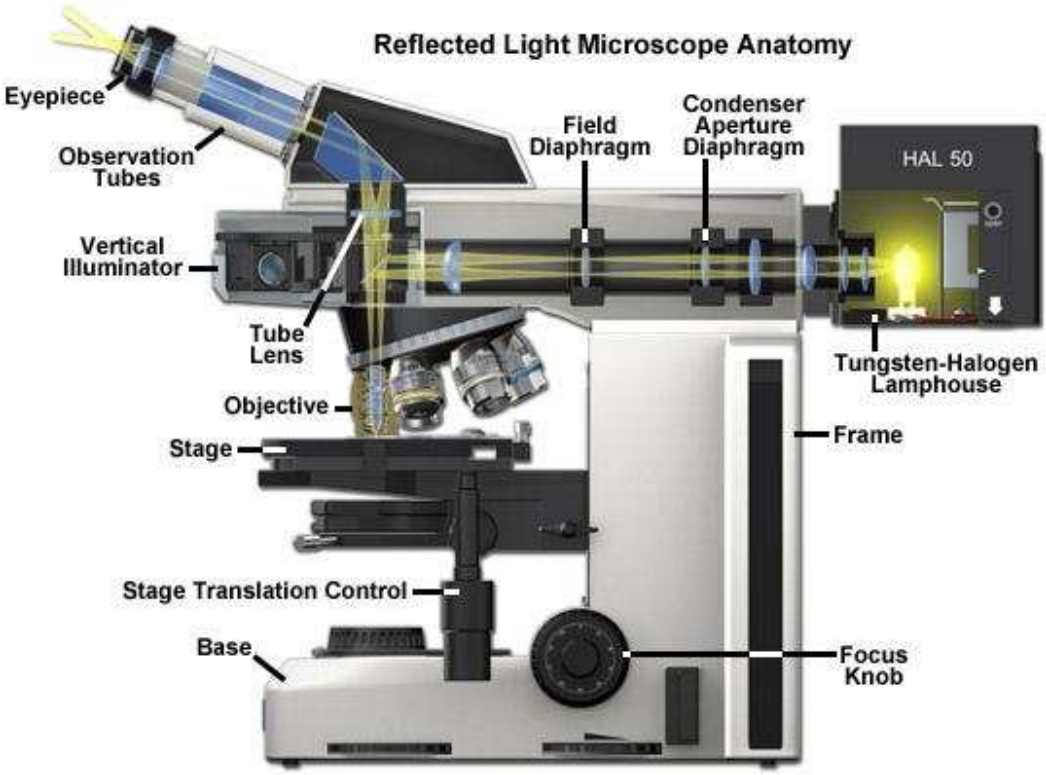

Figure 7: Schematic view of light optical microscope [20]

Most metals and alloys have a fine microstructure, so a light optical microscopy (LOM) is used to magnify and analyse the sample surface. Visible light illuminates the sample and a system of lenses is used to magnify the sample. Special microscopes are available for metal analysis which uses different modes to image the structure.

Bright field mode:
Is the most used mode and gives an overall image of the sample. The light beam hits the sample surface by 90℃ and is reflected. The co ntrast is given due to colour, reflectivity and roughness. The colour of the image corresponds to the colour of the phases.

Dark field mode:
The light beam hits the sample surface in low angles and so only light from scratches, grain boundaries, cracks, rough surfaces or holes reach the observer, the plane surface appears dark. This mode gives information about the quality of the surface polishing.

Difference interference mode:
This mode gives information about height differences in the sample surface. A pseudo-colour image is generated by the recombination of two light beams, which interfere via different path lengths caused by height difference.

Polarized image mode:
For Polarized image mode the microscope must be equipped with polarizers; one positioned in the light path somewhere before the specimen, and an analyser (a second polarizer), placed in the optical pathway between the objective rear aperture and the observation tubes or camera port. The polarized light beam hits the sample surface, is modified by the sample and reflected back to the analyser. Contrast is given according to the optical properties and the orientation of the sample; a pseudo-colour image is generated [21].
By rotating the sample the most striking effect becomes obvious: Low symmetry phases change their colour in more extends than high symmetry phases.

2.2.2 Scanning electron microscopy (SEM) & electron probe microanalysis (EPMA) [22, 23]

Scanning electron microscopy (SEM) has a better resolution than LOM and is often used similar to LOM. An electron beam is used instead of visible light; and since the wavelength of electrons is 100 000 times shorter than for visible light, SEM can reach magnifications up to 500 000x. SEM uses a scanning technique; an electron beam is focused by coils to less than 1µm spot size at the sample surface and scans an area of the sample. The electron beam impact on the sample gives rise to several processes, which are shown in Figure 8.

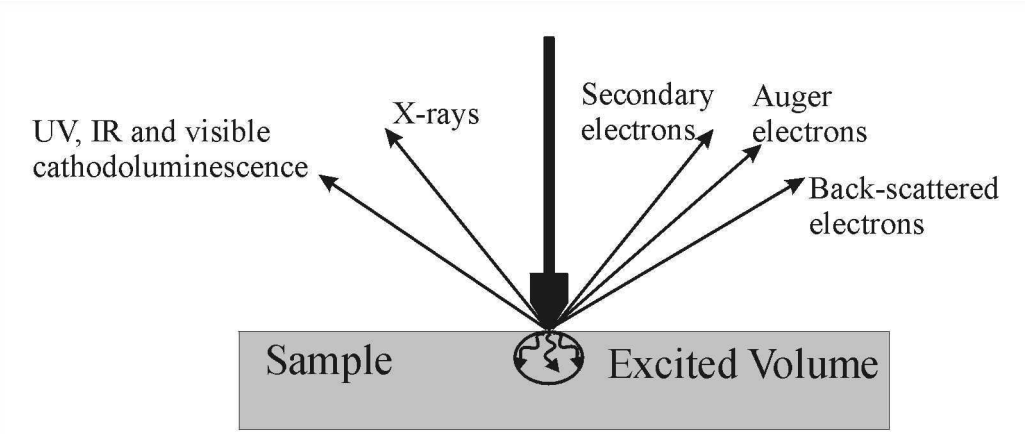

Figure 8: Effects after interaction of electron beam with sample [22]

The back-scattered electrons are analysed by the BSE-detector. An image is generated, whose contrast is due to the atomic number. This image is used to distinguish between phases with different composition.

Secondary electrons (SE) have much lower energy than BSE and generate an image which represents the topography of the sample surface.

Electron probe microanalysis (EPMA) uses the generated characteristic X-rays to analyse small spots of the sample. According to Mosely´s law the wavelength of the emitted X-rays depends on the atomic number. An energy-dispersive detector (EDX) or a wavelength-dispersive detector (WDX) analyses the X-rays.

Based on the BSE-image, different phases and their composition can be identified and analysed.

2.2.3 Powder X-ray diffraction (powder-XRD) [15, 16, 24-26]

Powder X-ray diffraction (XRD) is a commonly used method to identify phases in a sample. The powdered sample is hit by monochromatic X-rays (their wavelength is in the order of magnitude of the lattice spacing) and according to Bragg´s law the beam is diffracted at several angles. During the scan an X-ray detector rotates over the sample and measures the reflected X-ray intensity.

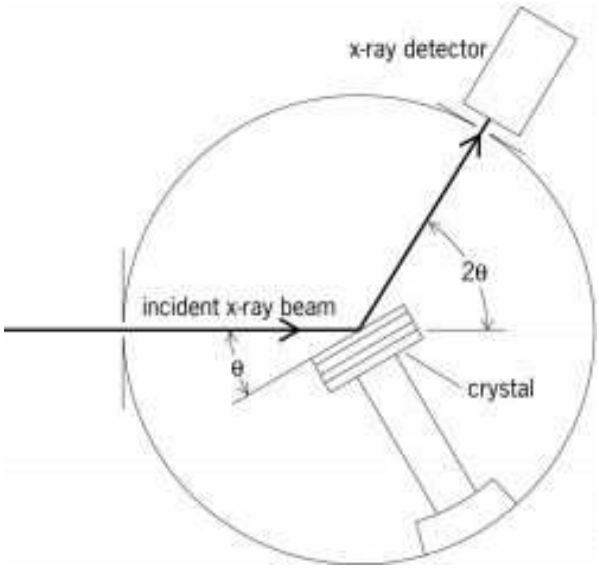

Figure 9: Setup of XRD with Bragg-Brentano pseudo focusing circle [27]

To generate X-rays, high energy electrons, emitted by a heated cathode and accelerated by a high voltage, hit the target material of the anticathode. The impact gives rise to several processes, among them the generation of the continuous spectrum and the characteristic radiation. The largest part of energy is converted to heat, which makes water cooling necessary

The slowing-down of the electrons via interaction with the electric field of the nucleus, leads to the emission of X-rays with a broad spectrum (“Bremsstrahlung”). If the applied voltage exceeds a value, characteristic for the target material, the characteristic radiation appears in addition to the continuous spectrum. Electrons in the inner K-Shell are excited by the incoming radiation and electrons from the outer shells can occupy their place. The energy difference is emitted in form of X-rays. Since only discrete transitions are allowed, the spectrum is quite sharp. It is possible to distinguish between the two different allowed transitions from the L-shell to the K-shell, resulting in $K\alpha_1$- and $K\alpha_2$-lines, and the transition from the M-shell to the K-

shell, resulting in the Kβ-line. The wavelength of the characteristic radiation depends on the material (Mosley´s law), usually copper is used for powder diffraction.
In a crystal structure it is possible to define lattice planes by means of the Miller indices. Father and son Bragg were the first who described the reflection pattern of an X-ray beam of a sample by means of lattice planes. Therefore the condition for constructive interference of an incident X-ray beam results in the Bragg equation:

$2d * \sin\theta = n * \lambda,$

where n is an integer, λ is the wavelength of incident wave, d is the spacing between the planes in the atomic lattice, and θ is the angle between the incident ray and the scattering planes. This equation is used for evaluation of the unit cell dimension. In non-primitve bravais lattices several X-ray reflections cannot be seen due to systematic extinction. This effect is useful for analysis.
The intensity **I** of a scattered reflex is given by:

$I_{hkl} = F_{hkl}^2 * M * LPG * A$

The structure factor **F** is probably the most important. It summarizes the information about position and species of the atoms in the unit cell. It also contains the correction for the displacement of the atoms due to thermal vibrations. The structure factor is given as

$$F_{hkl} = \sum_{j=1}^{N} f_j * e^{\frac{-B_j * \sin^2\Theta}{\lambda^2}} * e^{2*\pi*i*(hx_j + ky_j + lz_j)}$$

where f_j is the atomic form factor, B_j the temperature factor and x_j, y_j and z_j, are the position of the j-atom in the unit cell. The atomic form factor is equal to the atomic number for sin(θ)=0 and decreases with increasing angle. The temperature factor leads to a faster decrease with increasing angle.
The Multiplicity **M** is important to remember since there are several planes which lead to the same reflection angle.

The Lorentz-Polarisation-Geometry-factor **LPG** corrects the fact, that the X-ray beam is not strictly monochromatic and has a divergence. In addition an effect of polarisation during the scattering process is considered. In addition some geometry effects of the experimental setup are corrected.
The Absorption factor **A** corrects that parts of the X-rays are absorbed by the sample. It is mainly dependent on the absorption coefficient of the sample.
If all these factors are known, it would be possible to calculate the theoretic diffractogram and compare this to the measured one. But since not all factors are well-known or difficult to determine, the usual procedure in experiments is to fit a calculated diffractogram to the measured one. This is called Rietveld refinement. Usually the fit is a least square fit with a given set of parameters, such as the atom position in the unit cell, temperature factors etc.

2.2.4 Single crystal X-ray diffraction [15, 16, 24, 26, 28]

Single-crystal X-ray Diffraction is a non-destructive analytical technique which provides detailed information about the internal lattice of crystalline substances, including unit cell dimensions, bond-lengths, bond-angles, and details of site-ordering. Directly related is single-crystal refinement, where the data generated from the X-ray analysis is interpreted and refined to obtain the crystal structure.
The setup in single crystal X-ray diffraction (see Figure 10) is comparable to the powder diffraction setup. The X-rays are generated equal as in the powder-XRD. The sample consists of a single crystal that has been attached onto a thin glass fiber. The glass fiber has in turn been attached to a brass pin that is mounted on to the goniometer heads. Single crystal diffractometers use either 3- or 4-circle goniometers, which refers to the four angles that define the relationship between the crystal lattice, the incident ray and the detector (2θ, χ, φ, Ω). Furthermore, the crystal is centered within the X-ray beam before a measurement starts. When the X-rays hit the sample, they are either transmitted through the crystal, reflected of the surface or diffracted by the crystal lattice. Only diffracted rays are at the correct orientation for the configuration to be collected by the detector.
Different from Figure 10 an area detector (CCD) is nowadays used instead of a scintillation counter for detecting the diffracted X-rays. Charge coupled device (CCD) is a common technique used today for the transformation of X-ray photons into an electric signal which is sent to a computer for processing.

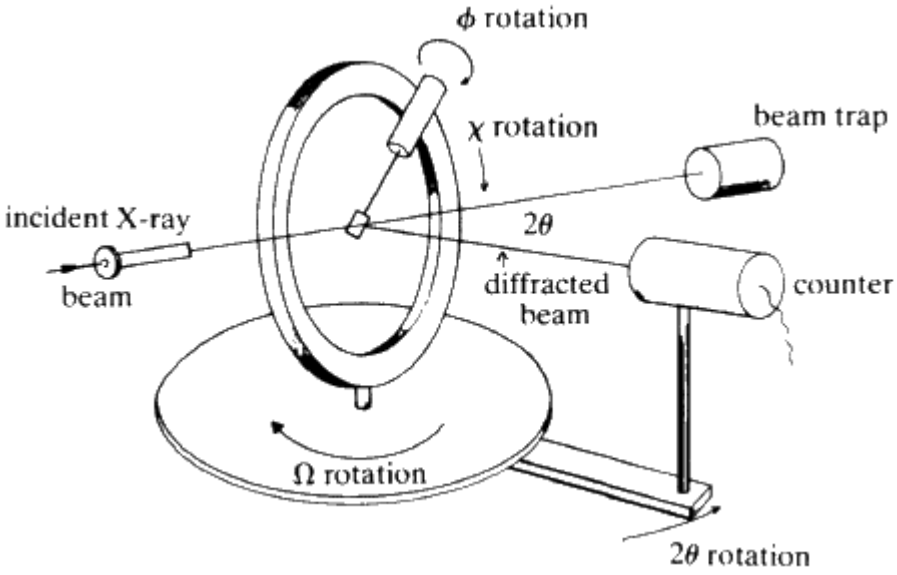

Figure 10: Setup of single crystal XRD [28]

The procedure for the data collection usually starts with a preliminary image to screen the sample quality and select parameters for further investigation. Through a short collection routine, a preliminary set of frames are collected for the determination of the unit cell. Reflections are auto-indexed, and a software selects a reduced primitive cell and calculates the orientation matrix that gives an initial position of the unit cell relative to the actual crystal position within the beam. Using least-squares method the new cell is refined to establish the final orientation matrix for the sample. Next data for intensity is collected using an incremental scan method for a sphere (or hemisphere) and this is the time consuming step in a complete measurement.

Least square methods are once again used to solve the phase problem (CCD detects only the intensity of the beam, not its phase which contains crucial information of the studied specimen) in order to find a unique set of phases that can be linked with the structure factor (a mathematical description of how a material scatters incident radiation) to determine the electron density. This in turn leads to the initial electron density map where different elements, depending on their atomic number, are assigned to different areas of the map to match with the intensities. Assigning elements to the different centers can be simplified if consideration is given to distances and angles to intensities. Once the crystal structure is solved it can be further refined according to the same procedure as explained in the powder-XRD diffraction.

2.2.5 Differential thermal analysis (DTA) [15, 16, 29]

Differential Thermal Analysis (DTA) is a dynamic standard technique that is helpful in detecting all phase transitions in a sample. A partial setup is shown in Figure 11 and includes thermocouples, furnace, a sample and a reference (in crucibles made of e.g. aluminum oxide). Moreover a temperature controller, cooling system and recording device is also needed. The furnace is symmetrical and contains two thermocouples; one for the sample crucible and the other for the reference which usually is an empty crucible. This closed setup allows for purging of the furnace to minimize oxidation of the sample before the temperature program can be started. During the measurement the temperature difference between the two crucibles is plotted against the temperature, where all deviation indicates a phase transition. The reason for this is because all first order phase transitions involves a heat exchange between the sample and the surrounding since bonds between atoms are formed or broken. Once the temperature has been evaluated for each phase transition they can be plotted in the phase diagram.

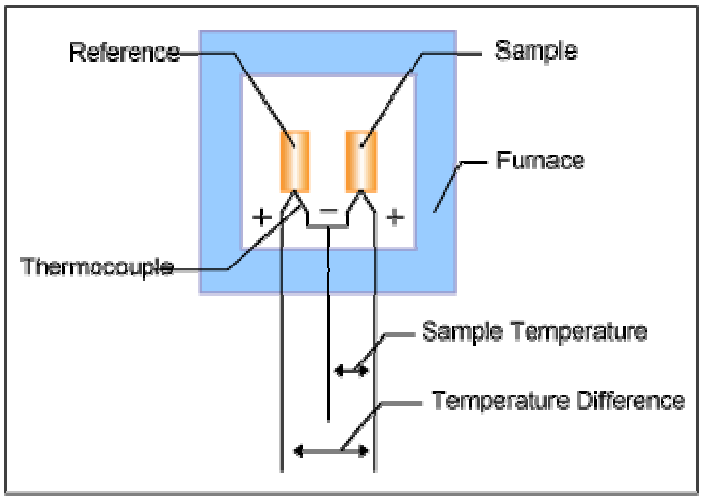

Figure 11: Principal setup of differential thermal analysis [30]

The temperature program usually includes a second heating/cooling cycle to check for reversibility of reactions. Thermal effects can sometimes be more intense during the second cycle and usually have to do with improved thermal contact of the re-solidified sample with the crucible. However, samples may have lost their thermodynamic equilibrium when entering the second cycle, especially if new effects appear and thus the first cycle is typically more reliable. Furthermore, two types of reactions are possible; invariant and non-invariant reactions. They give rise to

different peak shape and are illustrated in Figure 12. A sample with the composition X2 (red curve) is heated. At temperature T1 a steep and sharp peak is obtained as the whole transformation energy is consumed at this temperature (phase A+B transform into phase B+liquid) and hence the onset temperature is of interest. Further heating gives rise to a non-invariant reaction resulting in a maximum at T2 when all of the phase B has melted. A broad and flat shape is obtained in the second peak and temperature at the maximum would be the correctly evaluated temperature since this is the point where the non- invariant reaction comes to a halt. The blue curve (composition X1) represents the case of heating at the eutectic composition (congruent melting).

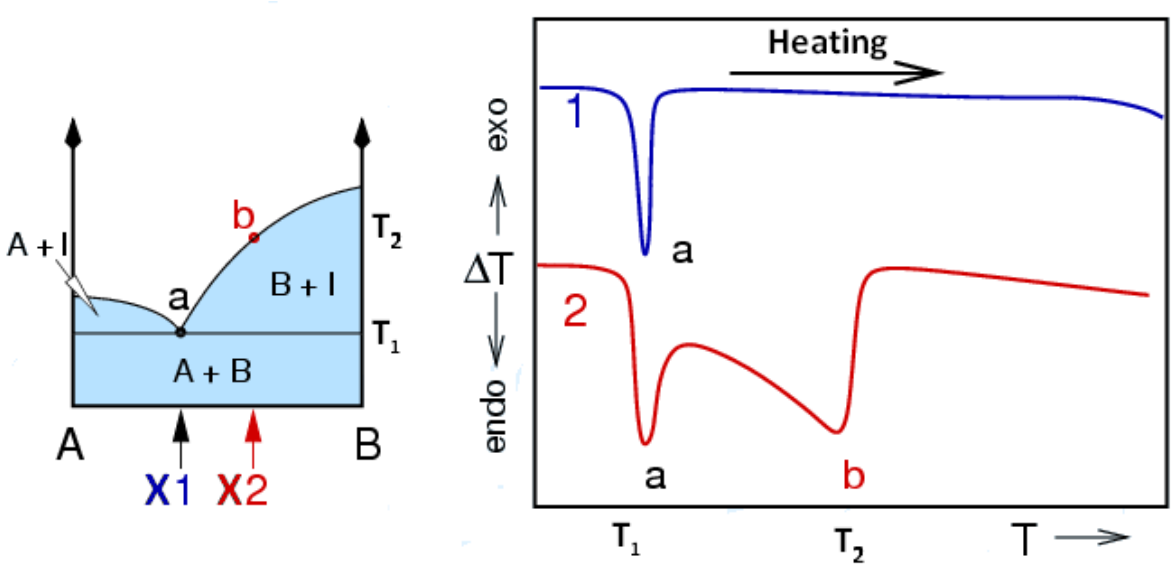

Figure 12: Binary phase diagram and reactions in DTA [31]

3 Literature

3.1 Au-Si

The binary Au-Si-system (see Figure 13) shows a simple eutectic phase diagram. Remarkable is the low eutectic point (363±3℃; 18.6 ±0.6at%Si), which is far away from the melting point of gold (1064℃) and silicon (1414℃). A lot of literature reports about this system, the presented phase diagram is based on a review of Okamoto and Massalski [32].

Metastable phases like $Au_{17}Si_3$ [33] , Au_5Si and Au_5Si_2 [32] are reported; they form at high quenching rates

The Au-Si-eutectic was one of the first metallic glass prepared by rapidly quenching of the liquid phase [11].

Strong Au-Si-interactions in the liquid are suspected to be responsible for the well stabilized liquid at the eutectic [34, 35]. This interaction leads to a short-range order in the liquid, which is confirmed by several methods like high energy XRD, neutron diffractions and ab-initio molecular dynamic studies.

The solubility of gold in the Si-phase and vice versa is very rare. No solid solubility of silicon in gold is indicated at the present phase diagram; whereas a small gold-solubility in silicon was reported to be at $2*10^{-4}$ at% [32].

Literature

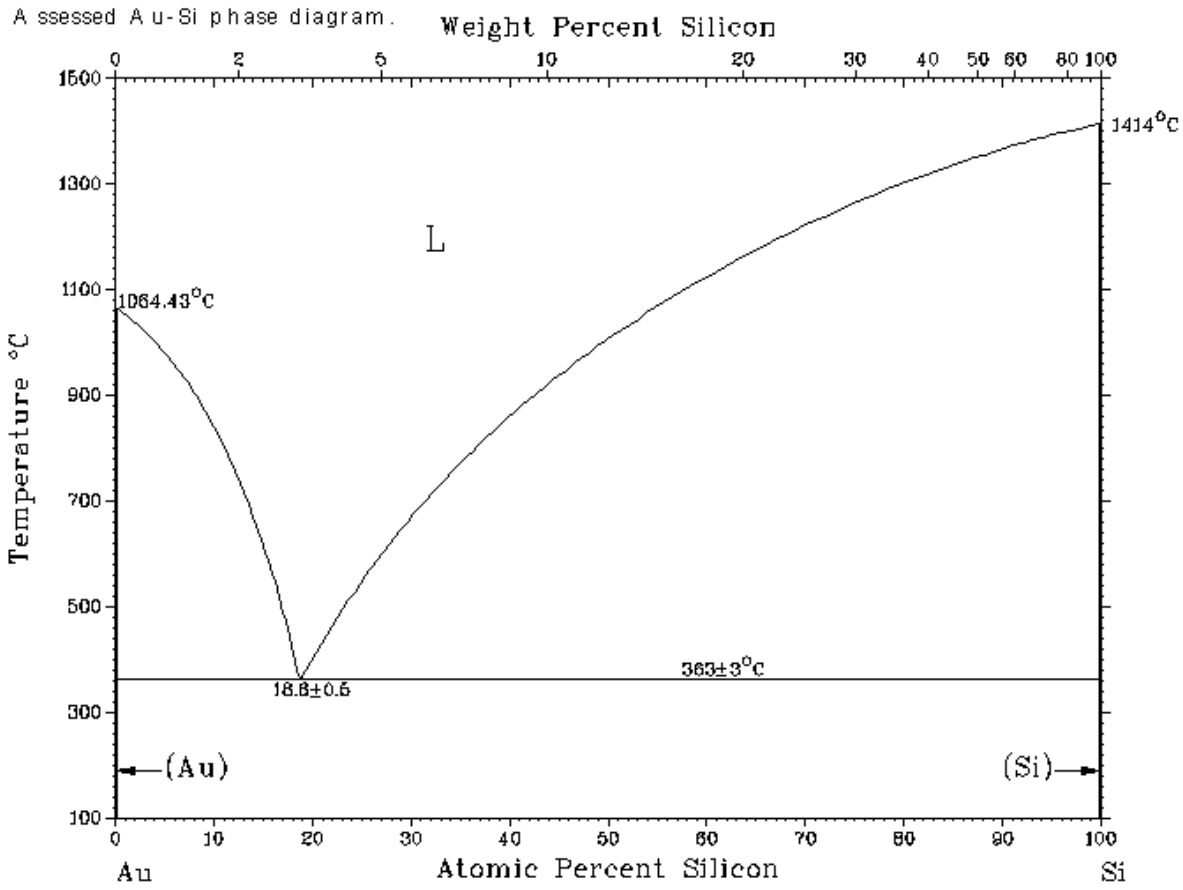

Figure 13: Binary phase diagram Au-Si [36]

Table 1: Phases of binary system Au-Si [32]

phase	space group	lattice parameter [Å]	pearson symbol
Au	$Fm\bar{3}m$	a=4.07894(5)	cF4
Si	$Fd\bar{3}m$	a=5.4306	cF8

Table 2: Reactions of binary system Au-Si [32]

reaction	composition (at% Si)			temp. (℃)	type
L ⇌ Au + Si	L:18.6±0.6	Au:0	Si: 100	363±3	eutectic

3.2 Au-Ni

The binary phase diagram of Au-Ni (see Figure 14) is a further simple system, given in Massalski´s handbook [36]. Although gold and nickel have the same crystal structure (cubic face centered), there is nearly no solubility into each other at room temperature. With higher temperatures the miscibility gap becomes smaller and ends with the critical point at 810.3℃ and 70.6at% Ni. The resulting solid solution has a melting point minimum at 955℃ and 42,5at% Ni.

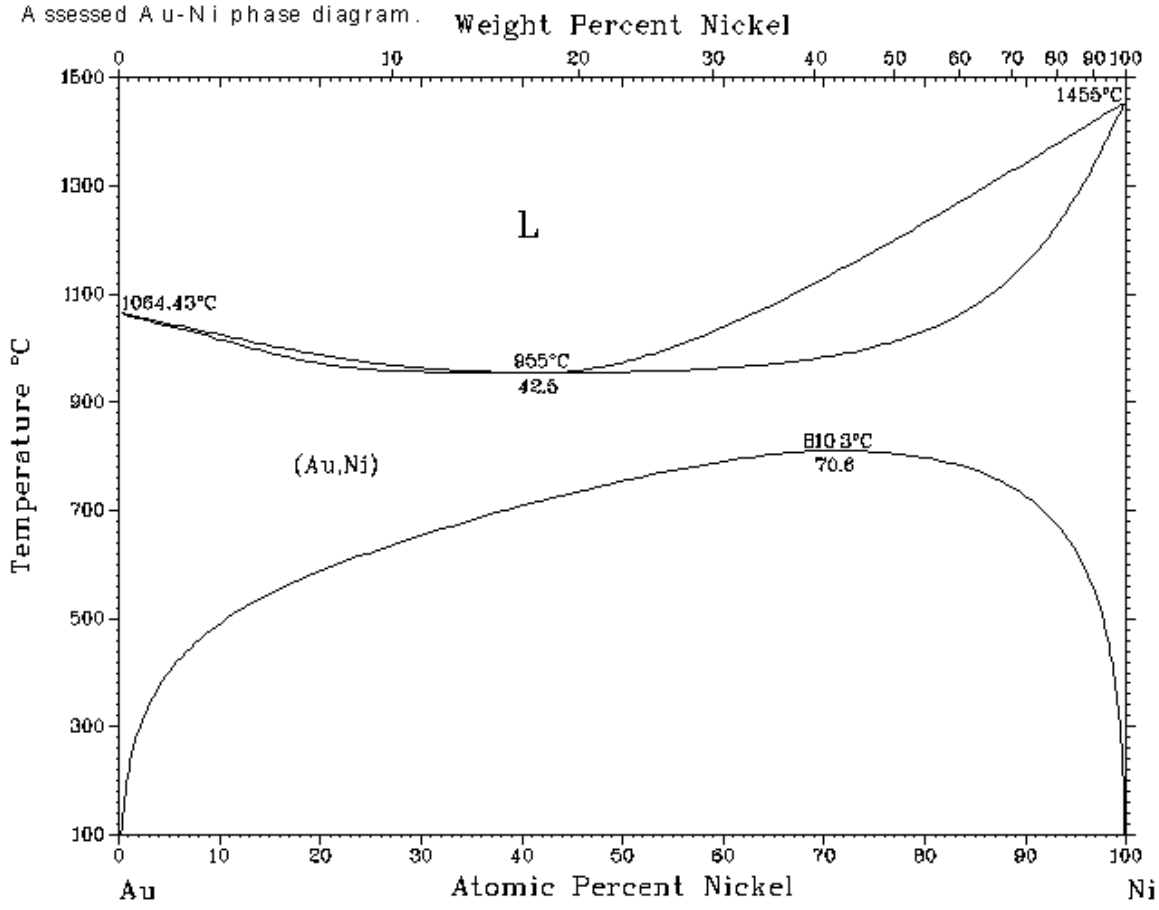

Figure 14: Binary phase diagram Au-Ni [36]

Table 3: Phases of binary system Au-Ni [37]

Phase	space group	lattice parameter [Å]	pearson symbol
Au	$Fm\bar{3}m$	a=4.07894(5)	cF4
Ni	$Fm\bar{3}m$	a=3.5241	cF4

Table 4: Reactions of binary system Au-Ni [37]

reaction	composition (at% Ni)			temp. (℃)	type
Au/Ni ⇌ Au + Ni	70.6	-	-	810.3	critical
L ⇌ Au/Ni	42.5			955	minimum

3.3 Ni-Si

The binary Ni-Si-system is more complex than the two other systems discussed before. There are six intermediate binary phases stable at room temperature and additional high-temperature modifications (see Table 5)[38]. As shown in Figure 15, there are several reactions, which are summarized in Table 6. The overall phase diagram in Figure 15 is given by Nash [38]. The allotropic transformations of Ni_3Si_2 and $NiSi_2$ were not confirmed by later authors [39, 40]. The grey marked region was re-investigated by Richter and the revised diagram is presented in Figure 16 [40]. The revised part of the phase diagram differs by reactions temperatures and there was no transformation of Ni_3Si_2 (ε/ε´) observed.

Table 5 lists the appearing phases and Table 6 gives an overview of all reactions in the binary phase diagram of Ni-Si.

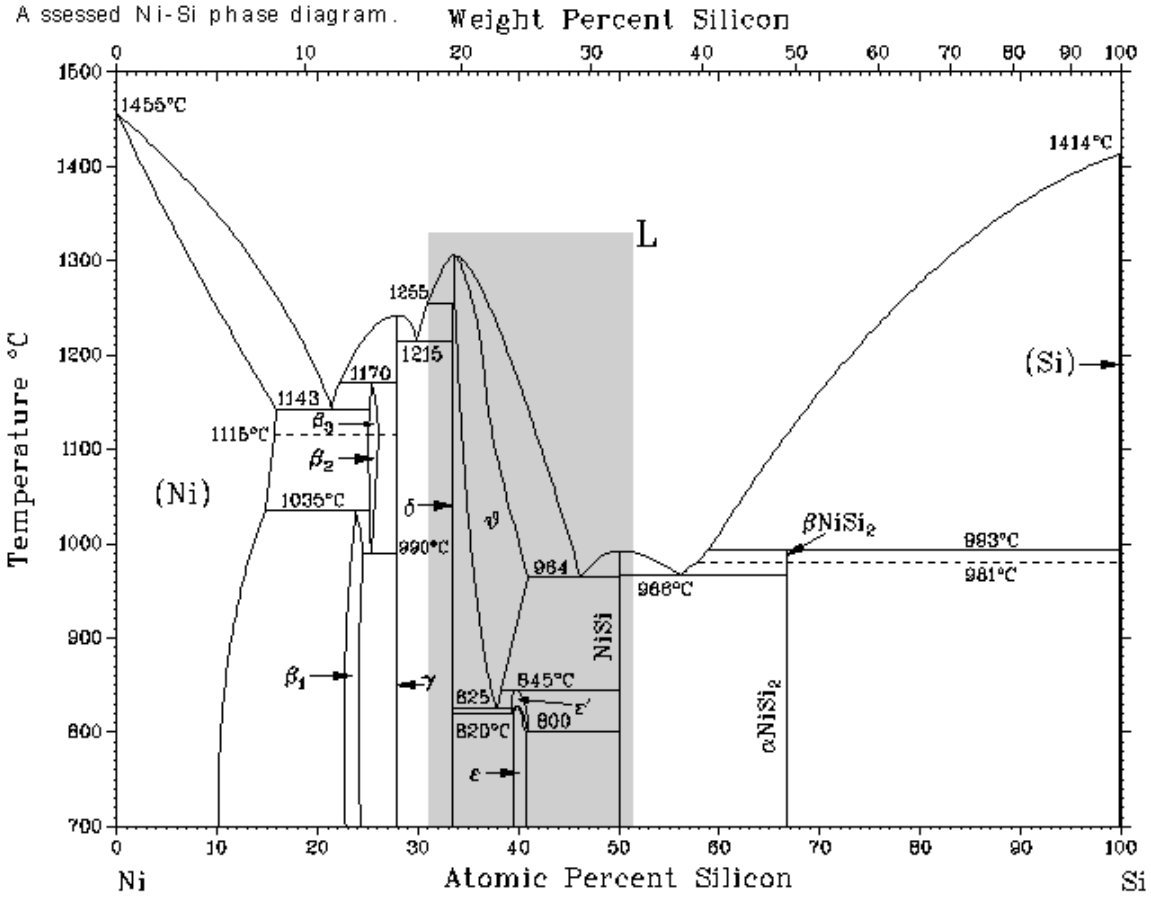

Figure 15: Binary phase diagram Ni-Si with revised grey field [36]

Literature

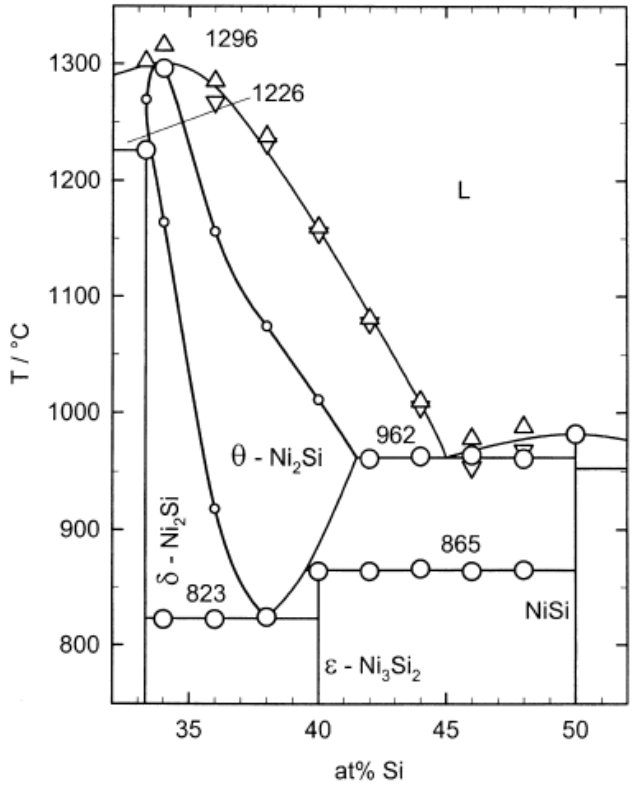

Figure 16: Revised section of Ni-Si-phase diagram by Richter [40]

Table 5: Phases of binary system Ni-Si [38, 40]

phase	space group	lattice parameter [Å]	pearson symbol
L			
(Ni)	$Fm\bar{3}m$	a=3.5241	cF4
β_1-Ni_3Si	$Fm\bar{3}m$	a=3.504	cP4
β_2-Ni_3Si	Pnma	a=5.50, b=6.50, c=4.35 [33]	oP16
β_3-Ni_3Si	-	-	-
$Ni_{31}Si_{12}$ (γ)	P321	a=6.67(1), c=12.28(8)	hP43
δ-Ni_2Si	Pnma	a=7.06, b=4.99, c=3.72	oP12
θ-Ni_2Si	$P6_322$	a=3.805, c=4.89	hP6
Ni_3Si_2	$Cmc2_1$	a=12.229, b=10.805, c=6.924	oC80
NiSi	Pnma	a=5.62, b=5.18, c=3.44	oP8
$NiSi_2$	$Fm\bar{3}m$	a=5.406	cF12
Si	$Fd\bar{3}m$	a=5.4306	cF8

Table 6: Reactions of binary system Ni-Si [38, 40]

reaction	composition (at% Si)			temp. (°C)	type
L ⇌ θNi_2Si	L:33,8	θ:33,8		1296	congruent
L + θ-Ni_2Si ⇌ δ-Ni_2Si	L:31,0	θ:33,6	δ:33,3	1226	peritectic
L ⇌ $Ni_{31}Si_{12}$	L:28,6	$Ni_{31}Si_{12}$:28,6		1246	congruent
L ⇌ $Ni_{31}Si_{12}$ + δ-Ni_2Si	L:29,6	$Ni_{31}Si_{12}$:28,6	δ:33,3	1215	eutectic
L + $Ni_{31}Si_{12}$ ⇌ β_3-Ni_3Si	L:32,2	$Ni_{31}Si_{12}$:28,6	β_3:25,0	1170	peritectic

$L \rightleftharpoons (Ni) + \beta_3\text{-}Ni_3Si$	L:21,3	Ni:17,0	β_3:25,0	1143	eutectic
$\beta_3\text{-}Ni_3Si \rightleftharpoons \beta_2\text{-}Ni_3Si$	25,0			1115	polymorphic
$(Ni) + \beta_2\text{-}Ni_3Si \rightleftharpoons \beta_1$	Ni:16,7	β_2:25,0	β_1:22,9	1035	peritectoid
$L + Si \rightleftharpoons NiSi_2$	L:60,4	100,0	$NiSi_2$:66,7	970	peritectic
$m\text{-}Ni_3Si \rightleftharpoons \beta_1 + Ni_{31}Si_{12}$	25,0	β_1:24,3	$Ni_{31}Si_{12}$:28,6	990	eutectic
$L \rightleftharpoons NiSi$	L:50,0	NiSi:50,0		989	congruent
$L \rightleftharpoons \theta\text{-}Ni_2Si + NiSi$	L:46,4	θ:39,8	NiSi:50,0	962	eutectic
$L \rightleftharpoons NiSi + NiSi_2$	L:55,6	NiSi:50,0	$NiSi_2$:66,7	948	eutectic
$\theta\text{-}Ni_2Si + NiSi \rightleftharpoons Ni_3Si_2(\varepsilon)$	θ:37,6	NiSi:50,0	Ni_3Si_2:40,0	865	peritectoid
$\theta\text{-}Ni_2Si \rightleftharpoons \delta Ni_2Si + Ni_3Si_2(\varepsilon)$	θ:36,7	δ:33,3	Ni_3Si_2:40,0	823	eutectoid

3.4 Au-Ni-Si

Information about the ternary Au-Ni-Si system is very rare; in literature only two papers could be found. One article [41] investigates epitaxy of gold on $NiSi_2$-layers and observed a solubility of gold up to 12at%. The presence of gold atoms in $NiSi_2$-structure is confirmed by the change in lattice parameter which is in accordance to Vegard´s law.

The other article [42] predicts an enlargement of the miscibility gap of the Au-Ni-system by addition of silicon. Therefore the invariant reactions $L \rightleftharpoons Au+Ni+ \beta_1\text{-}Ni_3Si$ and $L+Ni_{31}Si_{12} \rightleftharpoons Au+ \beta_1\text{-}Ni_3Si$ are assumed.

4 Experimental

4.1 Sample preparation

Samples were prepared by using exactly weighted pieces from a nickel sheet (Advent Research Materials, 99,99%), silicon lumps (99,9999%, Alfa Aesar) and gold granulates (99,99%, Ögussa). Samples were made with a mass of about 600mg, weighted on a Satorius microbalance R200D.

Samples were then prepared using arc-melting (MAM 1, Johanna Otto GmbH). The elements were melted in an argon atmosphere (Argon 5.0>99.999%). A copper plate cooled with water was the scene of the melting while the electrode was made of tungsten allowing for temperatures around 3000℃. A ll oxygen was removed through an evacuation and purging process with argon. Any remaining oxygen was removed with zirconium pieces that acted as oxygen getter. All samples were turned over and re-melted at least two times and once melted kept under the arc for at least 5 seconds each time to maximize the chances for proper homogenization. The weight loss was smaller than 1 mass-%, which is not significant enough to affect the sample composition.

After this most samples were placed in quartz glass tubes (only few as-cast- samples were investigated without annealing) and attached to a vacuum system. After evacuating and purging with argon (Argon 5.0>99.999%) the glass tube was evacuated once more below $4x10^{-3}$ mbar and then sealed using $H_2/0_2$ welding equipment. The sealed samples were heated in a muffle furnace (Nabertherm) according to different temperature programs (Table 7).

After the annealing process samples were quickly quenched in cold water to maintain the thermodynamic equilibrium achieved during annealing. All samples were subsequently crushed in a tungsten carbide mortar and two large pieces were saved for DTA and SEM analysis. The rest of the sample was further crushed into a powder for XRD investigation.

Some samples (nickel rich and gold rich) were too hard or too ductile to crush in the mortar. In this case, two pieces were cut for DTA and SEM analysis with a diamond saw. The rest was filed down with a diamond file and the resulting filings were investigated with XRD. Normally, a special heat treatment is used to secure that any lattice distortions, caused by the diamond file, would be healed. As the XRD-pattern showed good results this procedure was not necessary.

Experimental

The sample for DTA could be directly used for DTA measurements. A small piece yields good peak separation, a larger one has stronger signals. A good compromise was found with a mass about 100-150mg.

The pieces for SEM/EPMA-measurements needed further preparation. At first they were embedded using phenolic mounting resin with carbon filler (Struers PolyFast) in a heatable press (Struers LaboPress). The resin was heated to 180℃ for 5 minutes and cooled with water for another 3 minutes while a pressure of 15-20kN was applied during the entire procedure. A Metaserv 2000 polishing machine was used for grinding with SiC abrasive paper ranging from 600 to 1200 mesh and polishing with alumina powder with a particle size of 1 µm (Buehler, Micropolish II).

A summary of all sample preparation steps is illustrated in Figure 17 and Figure 18.

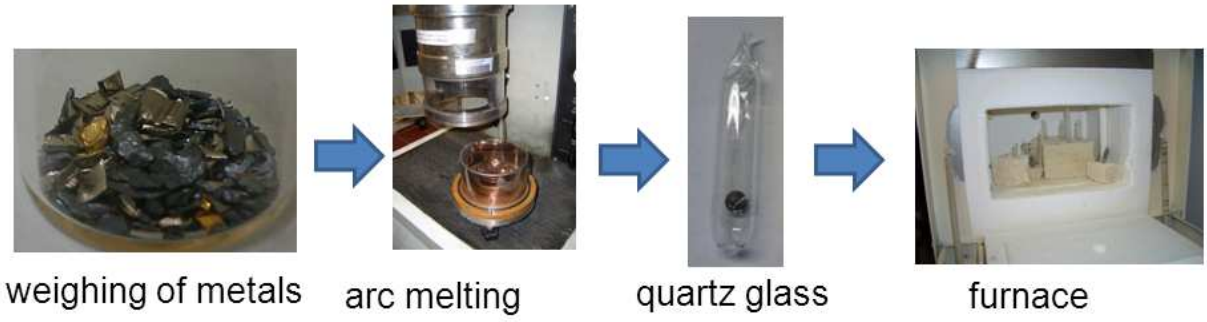

Figure 17: Sample preparation before annealing

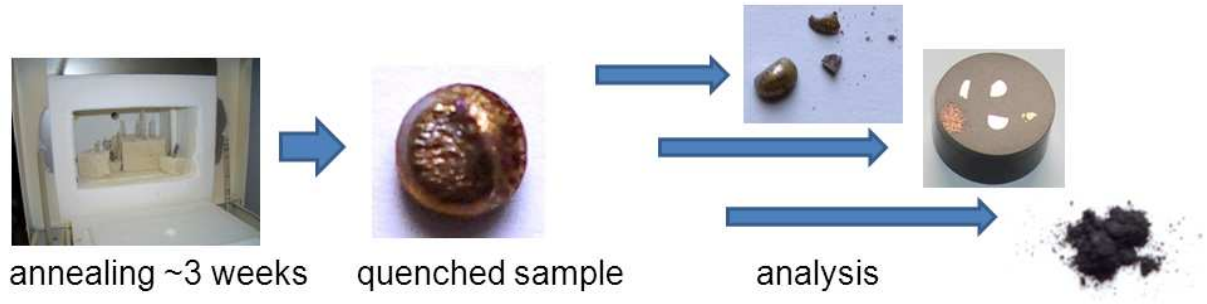

Figure 18: Sample preparation after annealing

4.2 Sample compositions

Different series of samples with reference to possible isopleths lead to samples with 15at% Ni (A-series), 30at% Ni (B-series), 60at% Ni (C-series) and 10at% Au (D-series). According to the amount of Nickel, the annealing temperature was 320℃ for the A-series, 500℃ for the B-samples and 700℃ for the C- and D-series.

The first sample series were prepared by Gabriel Reisinger, who investigated the samples A1-A7 and B1-B6 in his bachelor thesis “Untersuchungen im Phasendiagramm Au-Ni-Si” [43].

The analysis of these samples lead to the preparation of additional samples to analyse the two ternary phases and to place one sample per 3-phase-region.

Table 7 shows a detailed list of all samples containing the nominal composition in atomic percent, the composition according to the weighed portions and the temperature program applied to each. All samples are also drawn in a ternary plot in Figure 19.

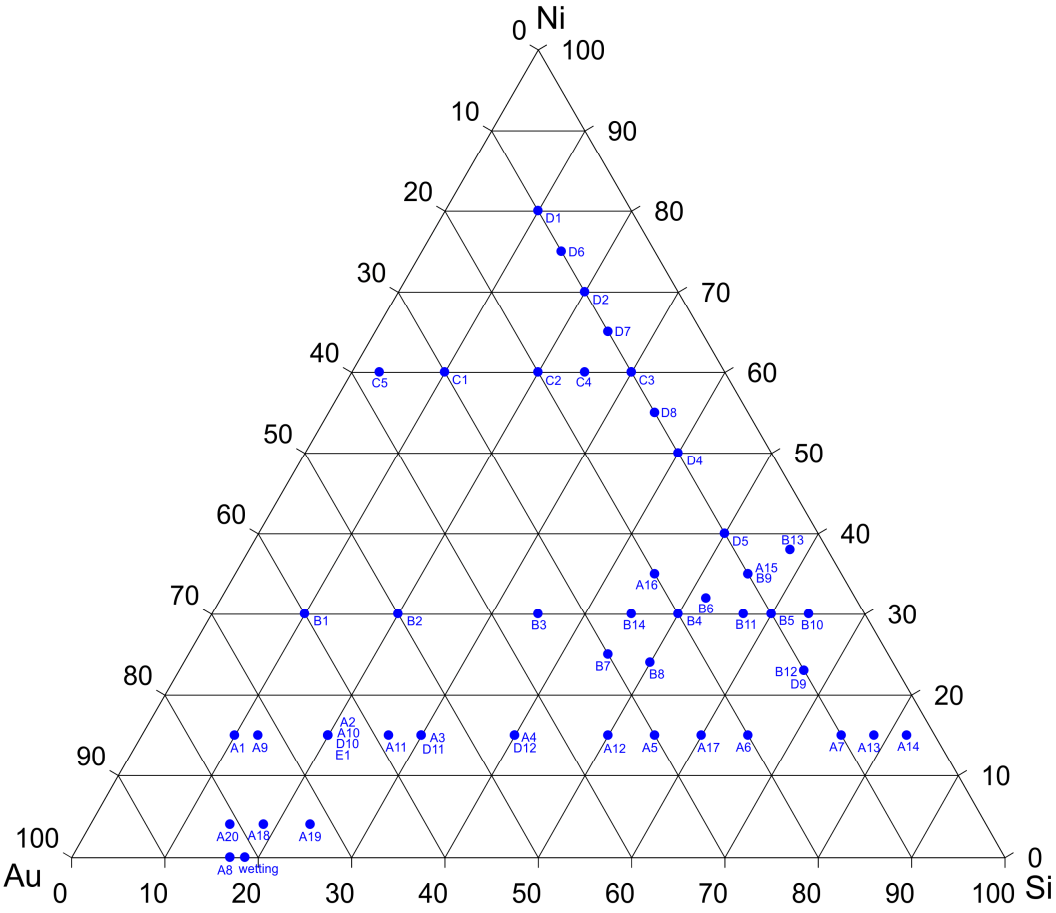

Figure 19: Prepared samples located in ternary phase diagram

Table 7: Overview of all prepared samples

Sample name	Nominal composition (at%)			Composition/weighed portions(at%)			Annealing temp. (℃)/duration
	Au	Ni	Si	Au	Ni	Si	
A1	75.00	15.00	10.00	75.06	14.99	9.95	320/24d
A2	65.00	15.00	20.00	64.90	15.01	20.09	320/24d
A3	55.00	15.00	30.00	55.12	14.95	29.93	320/24d
A4	45.00	15.00	40.00	44.95	15.07	39.97	320/24d
A5	30.00	15.00	55.00	30.01	14.96	55.03	320/24d
A6	20.00	15.00	65.00	20.00	15.02	64.98	320/24d
A7	10.00	15.00	75.00	10.01	15.02	74.97	320/24d
B1	60.00	30.00	10.00	59.96	30.09	9.95	500/17d
B2	50.00	30.00	20.00	49.94	30.03	20.03	500/17d
B3	35.00	30.00	35.00	35.01	29.96	35.03	500/17d
B4	20.00	30.00	50.00	20.04	30.00	49.96	500/17d
B5	10.00	30.00	60.00	10.00	30.05	59.95	500/17d
C1	30.00	60.00	10.00	29.96	60.02	10.02	700/17d
C2	20.00	60.00	20.00	19.99	60.05	19.96	700/17d
C3	10.00	60.00	30.00	9.99	60.02	29.99	700/17d
D1	10.00	80.00	10.00	10.01	80.05	9.94	700/17d
D2	10.00	70.00	20.00	10.02	70.01	19.97	700/17d
D3	10.00	60.00	30.00	9.98	60.00	30.02	700/17d
D4	10.00	50.00	40.00	10.01	49.99	40.00	700/17d
D5	10.00	40.00	50.00	10.00	40.02	49.98	700/17d
B6	16.00	32.00	52.00	16.33	31.76	51.92	500/21d
D6	10.00	75.00	15.00	10.03	74.89	15.09	700/21d
D7	10.00	65.00	25.00	9.97	65.02	25.02	700/21d
D8	10.00	55.00	35.00	10.05	54.95	35.00	700/21d
B7	30.00	25.00	45.00	30.15	24.98	44.87	500/24d
B8	26.00	24.00	50.00	26.03	24.07	49.89	500/24d
A8	83.00	0.00	17.00	83.07	0.00	16.93	500/3d
B9	10.00	35.00	55.00	9.96	34.72	55.33	500/21d
B10	6.00	30.00	64.00	6.03	29.93	64.04	500/21d
B11	13.00	30.00	57.00	12.90	29.84	57.26	500/21d
B12	10.00	23.00	67.00	10.06	22.95	67.00	500/21d
A9	72.50	15.00	12.50	72.51	15.28	12.22	500/4h, 320/21d
A10	65.00	15.00	20.00	65.39	14.96	19.65	500/4h, 320/21d
A11	58.50	15.00	26.50	58.82	14.76	26.42	500/4h, 320/21d
A12	35.00	15.00	50.00	35.01	15.03	49.95	500/4h, 320/21d
A13	6.50	15.00	78.50	6.42	14.90	78.68	500/4h, 320/21d
A14	3.00	15.00	82.00	2.95	15.03	82.02	500/4h, 320/21d
C4	15.00	60.00	25.00	15.00	60.09	24.91	700/21d
C5	37.00	60.00	3.00	36.87	60.10	3.03	700/21d

A15	10.00	35.00	55.00	10.00	35.00	55.00	500/3d, 320/21d
B13	4.00	38.00	58.00	3.98	37.83	58.18	500/21d
A16	20.00	35.00	45.00	19.97	34.93	45.09	500/3d, 320/21d
D9	10.00	23.00	67.00	10.06	22.95	67.00	700/7d
B14	25.00	30.00	45.00	25.03	30.15	44.83	500/4d
A17	25.00	15.00	60.00	25.12	14.81	60.06	500/14d, 320/1d
E1	65.00	15.00	20.00	64.90	15.01	20.09	900/3d
D10	65.00	15.00	20.00	64.90	15.01	20.09	700/1d
D11	55.00	15.00	30.00	55.12	14.95	29.93	700/1d
D12	45.00	15.00	40.00	44.95	15.07	39.97	700/1d
Wetting	81.40	0.00	18.60	81.34	0.00	18.66	as cast
A18	77.40	4.00	18.60	75.14	4.07	20.79	as cast
A19	72.40	4.00	23.60	72.93	3.89	23.18	as cast
A20	81.00	4.00	15.00	80.51	4.02	15.47	as cast

4.3 Experimental Procedures, Sample Analysis

4.3.1 Light optical microscopy (LOM)

The LOM (Zeiss Axiotech 100) was used to check the quality of the embedded samples prior to SEM investigation and to check for phases exhibiting any polarizing properties. For special samples, e.g. samples in eutectic regions, metallographic investigation were used to check microstructures and evaluate the homogeneity of samples.

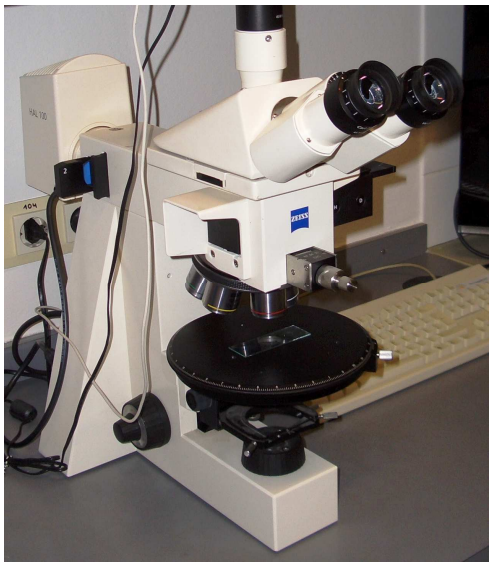

Figure 20: Zeiss Axiotech 100 microscope

4.3.2 Scanning electron microscopy

The freshly polished samples were investigated with a Zeiss Supra 55VP SEM for identification of present phase equilibrium and quantitative analysis of the composition. All detectors are built by Oxford Instruments. SE and BSE imaging modes were used as well as quantitative EDX analysis. The acceleration voltage used for EDX was 20kV (10nA/120µm collimator). Cobalt acted as a standard to control parameters of the measured beam such as current and resolution. Calibration was done with samples of pure gold, nickel and silicon.

Figure 21: Zeiss Supra 55VP SEM/EPMA

4.3.3 Powder X-ray diffraction (powder-XRD)

For powder X-ray analysis a Bruker D8 ADVANCE system was used (r = 217.5mm). The X-ray source origins from a copper X-ray tube (1.534753 Å, 40kV, 40mA) while the detector used was a LynxEye position sensitive detector capable of a simultaneous measurement of ~3° to minimize measuri ng time. The instrument, set in a Bragg-Brentano reflection (θ/2θ geometry), collected reflections with a step size of 0.0103° for an overall counting time of either a pproximately 30 min or 1 hour.

Before each measurement the samples were powdered with a tungsten carbide mortar or a diamond file. The powder was applied on a silicon single crystal sample holder covered with grease (Vaseline) that has been dissolved in cyclohexane. For Rietveld refinement and further analysis of the obtained diffractograms the Software TOPAS was used. Upon availability, structural information was gathered from literature.

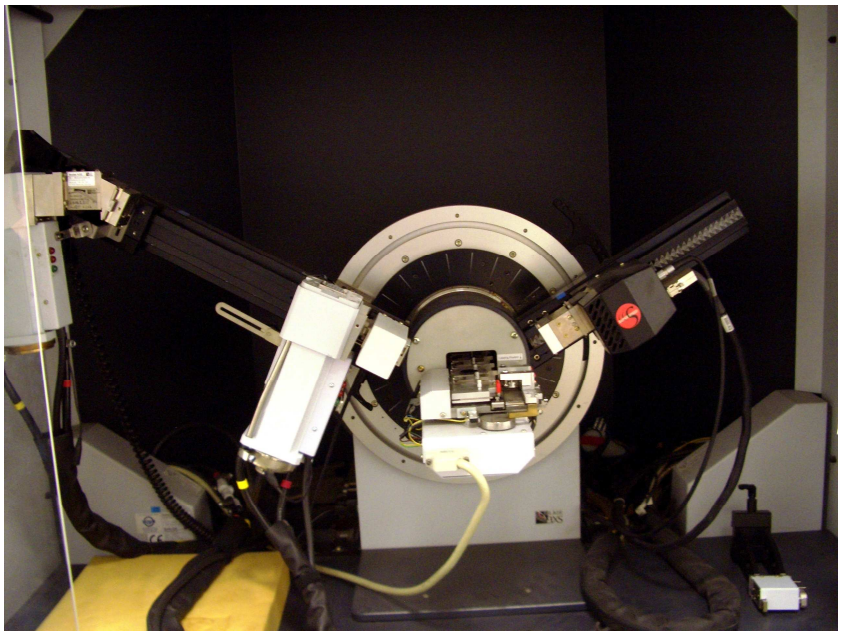

Figure 22: Powder-XRD BRUKER D8

4.3.4 Single crystal X-ray diffraction

For single crystal measurements the intensity was recorded on a Bruker Nonius KappaCCD FR590 four circle diffractometer equipped with a CCD detector and a 300µm capillary-optics collimator (Mo tube 0.71073 Å, graphite monochromator). The crystal-to-detector distance was 30mm and data was collected 3-70° (2 θ). The acquisition time per frame was 250s/° in ω. The result was later processed with SHELXL software.

Figure 23: Single crystal-XRD Bruker Nonius KappaCCD FR590

4.3.5 Differential thermal analysis (DTA)

The main DTA used for temperature information on phase transitions was a Setaram Setsys Evolution TGA & DTA 2400. The thermocouple used was a type-S which consists of platinum and platinum90/rhodium10 making it suitable for temperatures up to 1600℃. For calibration standards of gold, tin and silicon were used. All samples (30 to 150mg) were heated in open alumina crucibles after evacuating and purging the system three times. During the following two heating and cooling cycles (Figure 25) a permanent argon flow was applied. After purging the sample was heated up rapidly to the corresponding annealing temperature of the sample. After equilibration the two DTA-cycles were applied. The heating and cooling rate was always 5K/min and the final temperature for each sample was slightly above the estimated melting point. Samples B3 and B8 were additionally measured with a Netzsch DTA 404 PC to countercheck the yielded reaction temperatures, but no significant difference was observed.

Figure 24: DTA-instrument Setaram Setsys Evolution TGA & DTA 2400

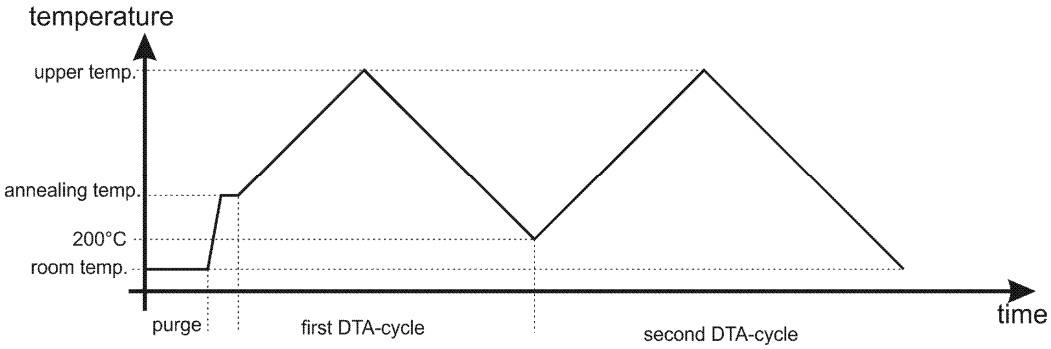

Figure 25: temperature program for DTA-measurement

5 Results and discussion

All presented isothermal sections, ternary phase diagrams, liquidus surface projection and isopleths were plotted in atomic percent.

5.1 Isothermal sections

5.1.1 Isothermal section at 320℃

The first samples annealed at 320℃ (in particular A4-A7) were not in equilibrium. They did not contain τ_1 and τ_2, which were originally obtained at 500℃ (later the stability at 320℃ was confirmed). It was necessary to anneal these samples primary at 500℃ to form τ_1 and τ_2, then cool them slowly to 320℃ and keep them there (see 5.2). One of these special-treated samples was A16; Figure 26 shows the SEM- and LOM-image of it.

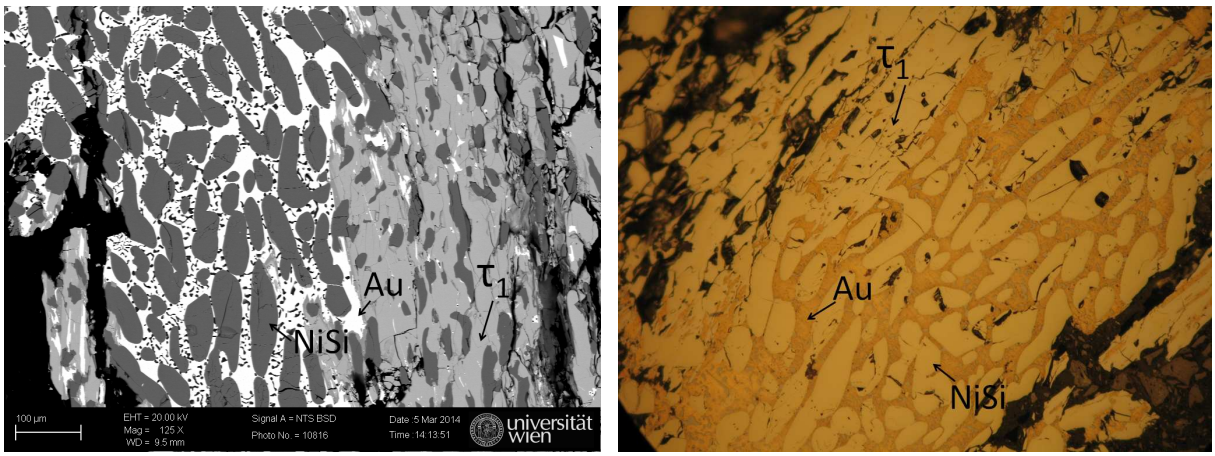

Figure 26: Sample A16 – left: SEM-image, right: LOM-image

Figure 27 presents the isothermal section at 320℃. There are four 3-phase-fields and one 2-phase-field obtained from the results of the SEM/EPMA-analysis of the samples. Another six 3-phase-fields which are not confirmed by experiments (dashed line) are proposed according to sections at higher temperature.

Compared to the phase composition of binary components from literature (stoichiometric composition) the measured values by EPMA-methods differ up to 1%. This is within the accuracy of the measurements and so the corresponding stoichiometric composition in the isothermal section was used.

The results of the XRD-measurements agree with the SEM-measurement.

As expected, there was no liquid phase in this isothermal section; the addition of Nickel does not lead to a lower melting temperature than in the binary Au-Si-system.

The $NiSi_2$-phase shows a gold-solubility of 1.5%. A higher solubility of gold in the $NiSi_2$-phase as described in [41] was not observed.

Table 8 shows selected data of the phase-composition obtained from the SEM/EPMA-analysis and the XRD-analysis. A minimum of 3 different points per phase-analysis with the microprobe was aimed to get a reliable average value of the composition. The total weight-percentage of all EPMA-measurements was checked and was adequate (99-102wt%).

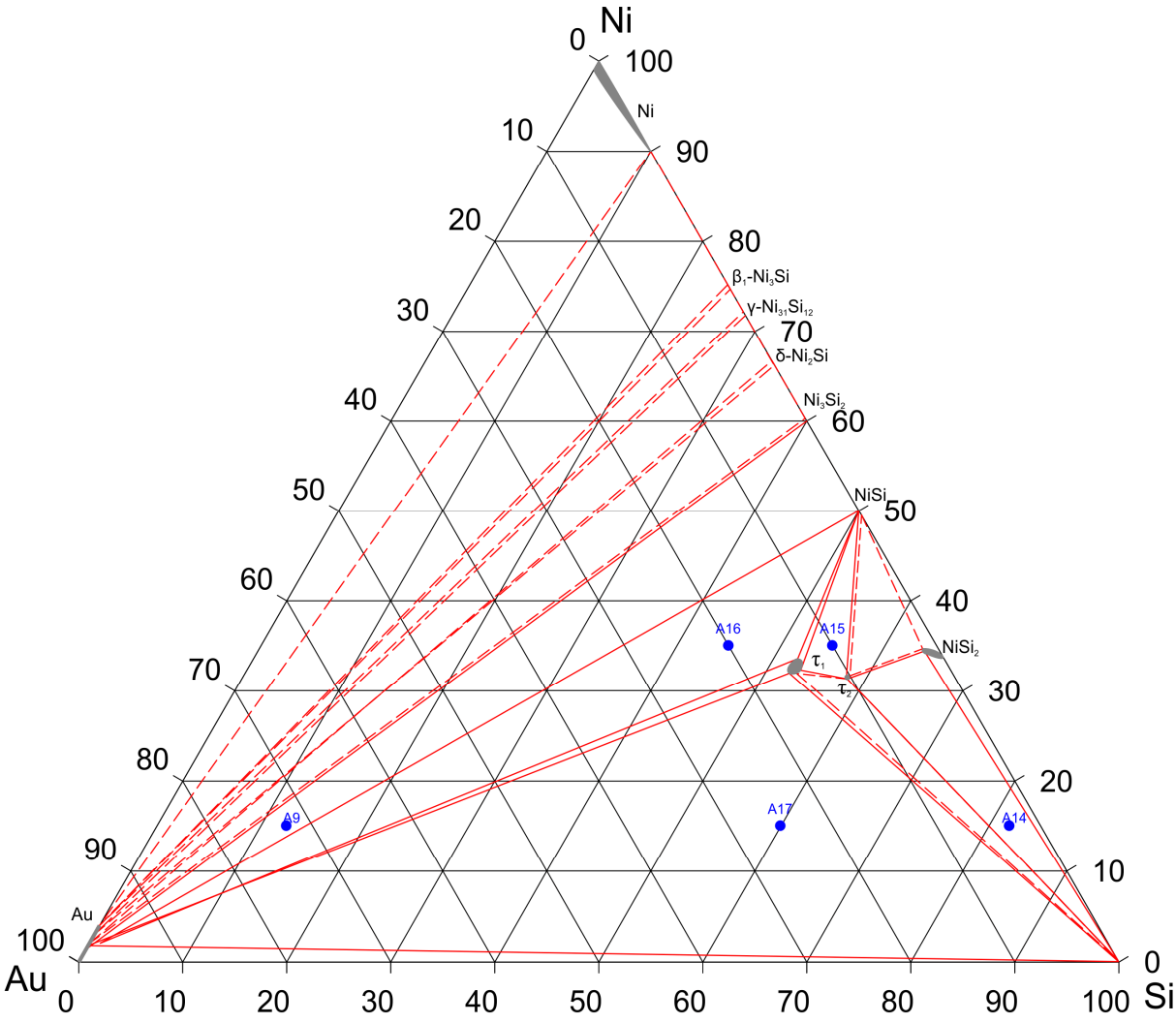

Figure 27: Isothermal section at 320℃; dashed line s are not confirmed by experiments

Table 8: Experimental data of XRD- & EPMA-analysis at 320℃

name/annealing composition	**XRD**		**SEM (at%)**		
	phase	lattice parameter	Si	Ni	Au
		Au-Ni_3Si_2			
A9 / 320°C	(Au)	a=4.079(1)	0.0	0.9	99.1
Au72.5Ni15Si12.5	Ni_3Si_2	a=12.356(7); b=10.712(5); c= 6.940(3)	41.1	58.7	0.2
		Au-NiSi-τ_1			
A16 / 320°C	(Au)	a=4.079(1)	1.0	2.1	96.9
Au20Ni35Si45	NiSi	a= 5.184(1); b=3.335(1); c=5.619(1)	50.6	49.4	0.0
	τ_1	a=12.783(1); b=3.774(1); c=7.975(1); β=109.927(2)	51.7	35.0	13.3
		$NiSi_2$-Si-τ_2			
A14 / 320°C	$NiSi_2$	a=5.416(1)	64.1	34.4	1.5
Au3Ni15Si82	Si	a=5.431(1)	99.8	0.2	0.0
	τ_2	a=3.766(1); b=33.843(1)	58.3	31.3	10.4
		NiSi-τ_1-τ_2			
A15 / 320°C	NiSi	a= 5.192(1); b=3.338(1); c= 5.631(1)	50.7	49.3	0.0
Au10Ni35Si55	τ_1	a= 12.820(2); b=3.769(1); c= 7.979(1); β=110.101(13)	53.6	32.1	14.3
	τ_2	a= 3.777(1); c=33.892(4)	58.1	31.4	10.5
		Au-Si-τ_1			
A17 / 320°C	(Au)	a=4.079(1)	0.0	1.8	98.2
Au25Ni15Si60	Si	a= 5.432(1)	99.9	0.1	0.0
	τ_1	a= 12.783(1); b=3.773(1); c=7.976(1); β=109.924(7)	52.3	32.0	15.7

5.1.2 Isothermal section at 500℃

In this sample series the new ternary phases τ_1 and τ_2 were observed for the first time. After the single-crystal-analysis and with the data of the ternary-phase-composition some specific samples were placed to explore the 3-phase-fields involving the ternary phases. The annealing conditions (500℃, 3 weeks) were adequate to form both phases and the samples were in equilibrium.

As expected, many samples at 500℃ contain the liqu id phase (Figure 28 shows the SEM-image and the LOM-image of sample B4. It contains also some Si-crystals, because the composition is close to the 3-phase-region L-τ_1-Si).

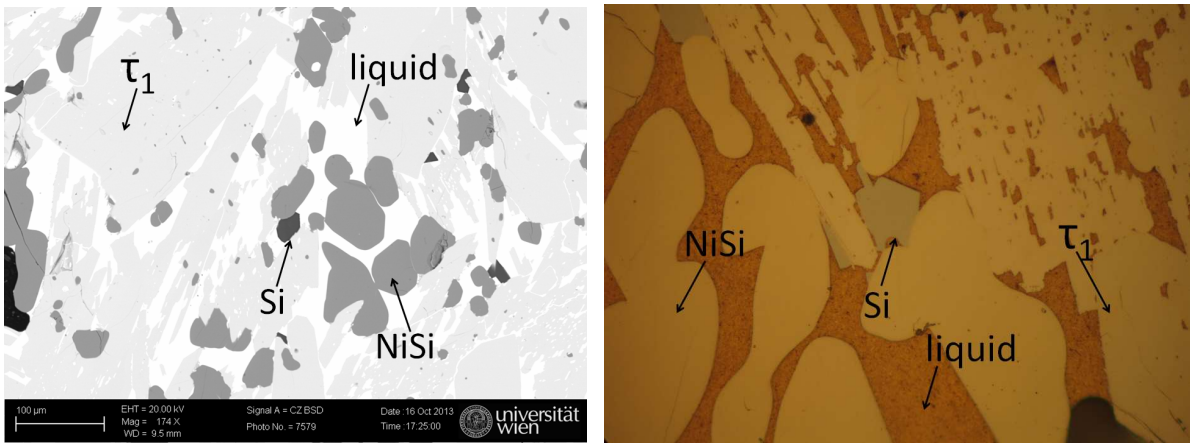

Figure 28: Sample B4 – left: SEM-image, right: LOM-image

The liquid phase composition is nearly the same as the binary Au-Si-eutectic; only a very small Ni-solubility (0.12%) was observed. To get a representative result of the composition by EPMA-analysis, the liquid phase fields were measured with an area scan.

Figure 29 shows the isothermal section at 500℃. Ei ght 3-phase-fields and two 2-phase-fields were obtained from the results of the SEM/EPMA-analysis of the samples, and another four 3-phase-fields which are not confirmed by experiments (dashed line) are proposed.

Table 9 shows selected data of the phase-composition obtained from the SEM/EPMA-analysis and XRD-analysis.

Table 9: Experimental data of XRD- & EPMA-analysis at 500℃

name/annealing composition	XRD		SEM (at%)		
	phase	lattice parameter	Si	Ni	Au
		Au-Ni_3Si_2-NiSi			
B2 / 500°C Au50Ni30Si20	(Au)	a=4.079(1)	0.0	4.0	96.0
	Ni_3Si_2	a= 12.458(9); b=10.808(7); c= 6.890(4)	41.4	58.4	0.2
	NiSi	a=5.121(11); b=3.484(7); c=5.641(14)	49.2	49.9	0.9
		Au-L-NiSi			
B3 / 500°C Au35Ni30Si35	(Au)	a= 4.079(1)	0.0	3.6	96.4
	L	-	15.7	0.0	84.3
	NiSi	a= 5.184(1); b=3.336(1); c=5.618(1)	51.1	48.9	0.0
		L-NiSi-τ_1			
B4 / 500°C Au20Ni30Si50	L	-	16.3	0.0	83.7
	NiSi	a= 5.182(1); b=3.336(1); c=5.618(1)	50.8	49.2	0.0
	τ_1	a=12.782(1); b=3.774(1); c=7.975(1); β=109.925(1)	52.1	31.6	16.3
B14 / 500°C Au25Ni30Si45	L	-	17.1	0.3	82.6
	NiSi	a= 5.183(1); b=3.336(1); c=5.616(1)	50.6	49.4	0.0
	τ_1	a=12.781(1); b=3.774(1); c=7.975(1); β=109.922(2)	52.0	31.8	16.2
		L-Si-τ_1			
B8 / 500°C Au26Ni24Si50	L	-	18.7	0.0	81.3
	Si	a= 5.430(1)	100.0	0.0	0.0
	τ_1	a=12.778(1); b=3.773(1); c=7.973(1); β=109.930(1)	52.2	32.0	15.8
		NiSi-τ_1-τ_2			
B9 / 500°C Au10Ni35Si55	NiSi	a= 5.189(1); b=3.340(1); c=5.624(1)	50.7	49.3	0.0
	τ_1	a= 12.806(2); b=3.770(1); c= 7.975(1); β=110.088(13)	52.5	32.2	15.3
	τ_2	a= 3.775(3); c=33.869(3)	57.7	31.7	10.6
		$NiSi_2$-Si-τ_2			
B10 / 500°C Au6Ni30Si64	$NiSi_2$	a= 5.427(1)	63.5	34.5	2.0
	Si	a= 5.419(1)	99.7	0.3	0.0
	τ_2	a=3.766(1); c=33.837(1)	58.1	31.4	10.5
		Si-τ_1-τ_2			
B11 / 500°C Au13Ni30Si57	Si	a= 5.432(1)	99.2	0.7	0.1
	τ_1	a=12.789(1); b=3.773(1); c=7.974(1); β=109.978(4)	53.4	32.1	14.5
	τ_2	a= 3.770(1); c=33.840(3)	58.3	31.2	10.5

B12 / 500°C	Si	a=5.431(1)	99.8	0.2	0.0
Au10Ni23Si67	τ_1	a=12.784(1); b=3.773(1); c=7.971(1); β=109.949(4)	53.1	31.9	15.0
	τ_2	a= 3.767(1); c=33.837(2)	58.4	31.0	10.6
		NiSi-NiSi$_2$-τ_2			
B13 / 500°C	NiSi	a= 5.183(1); b=3.334(1); c=5.619(1)	50.8	49.2	0.0
Au4Ni38Si58	$NiSi_2$	a=5.421(1)	64.1	34.5	1.4
	τ_2	a=3.766(1); c=33.836(1)	58.0	31.6	10.4
		Au-Ni$_3$Si			
B1 / 500°C	(Au)	a= 4.070(1)	0.0	6.1	93.9
Au60Ni30Si10	Ni_3Si	a= 3.524(1)	25.2	71.8	3.0
		L-τ_1			
B7 / 500°C	L	-	17.1	0.1	82.8
Au30Ni25Si45	τ_1	a=12.781(1); b=3.773(1); c=7.974(1); β=109.926(1)	51.9	31.9	16.2

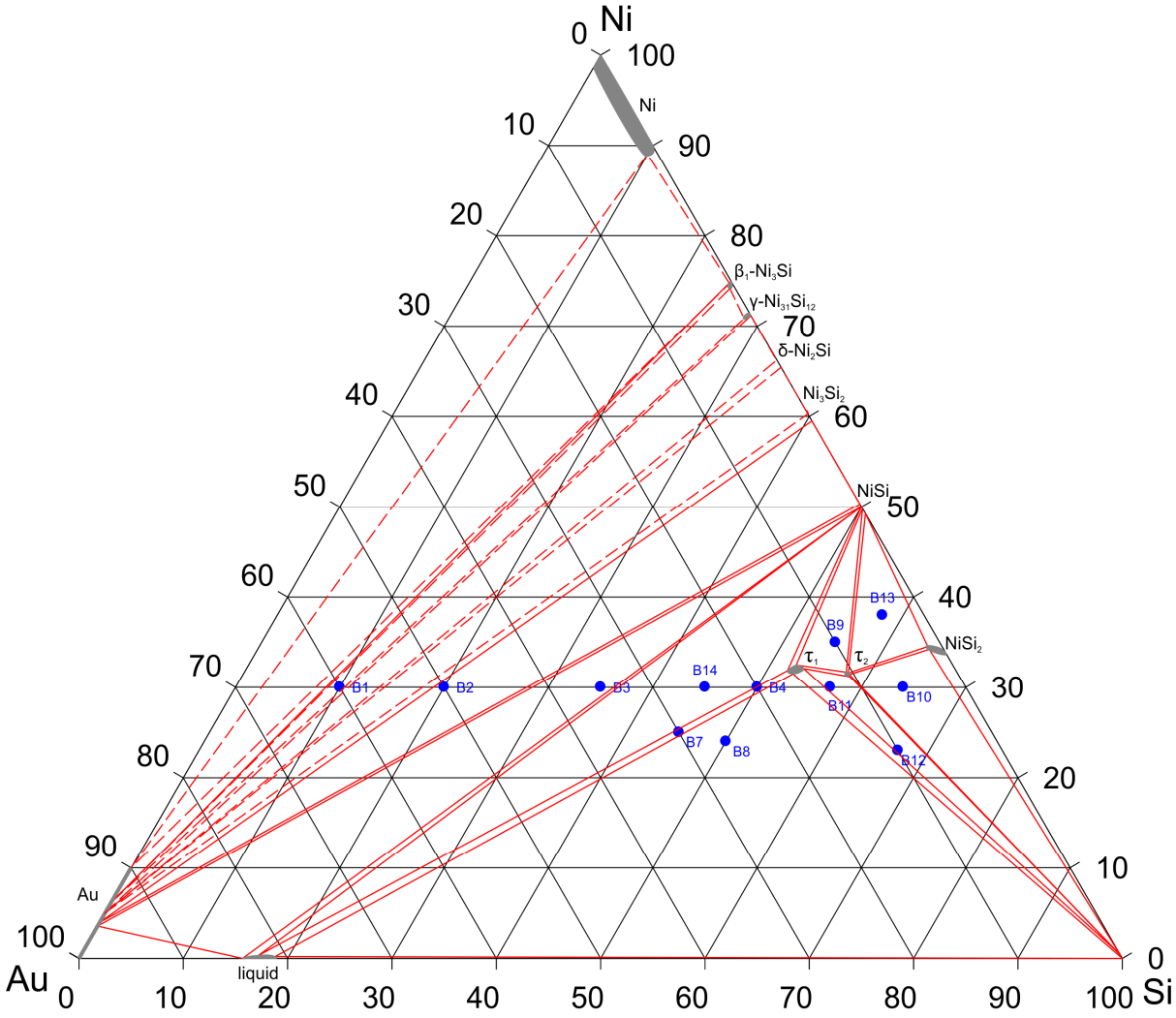

Figure 29: Isothermal section at 500℃; dashed line s are not confirmed by experiments

5.1.3 Metastable phase $Au_{17}Si_3$

In the course of investigating the samples containing a liquid phase, it was confirmed that a metastable phase with the composition Au85Si15 ($Au_{17}Si_3$) exists. Due to time restrictions this phase was not investigated further, but a sample was prepared to get the XRD-pattern.

Figure 30 presents the XRD-analysis from sample B3 in the three phase field Au-NiSi-liquid. The refinement of the XRD-pattern with structural data of gold and NiSi points out, that there is a third crystal structure present.

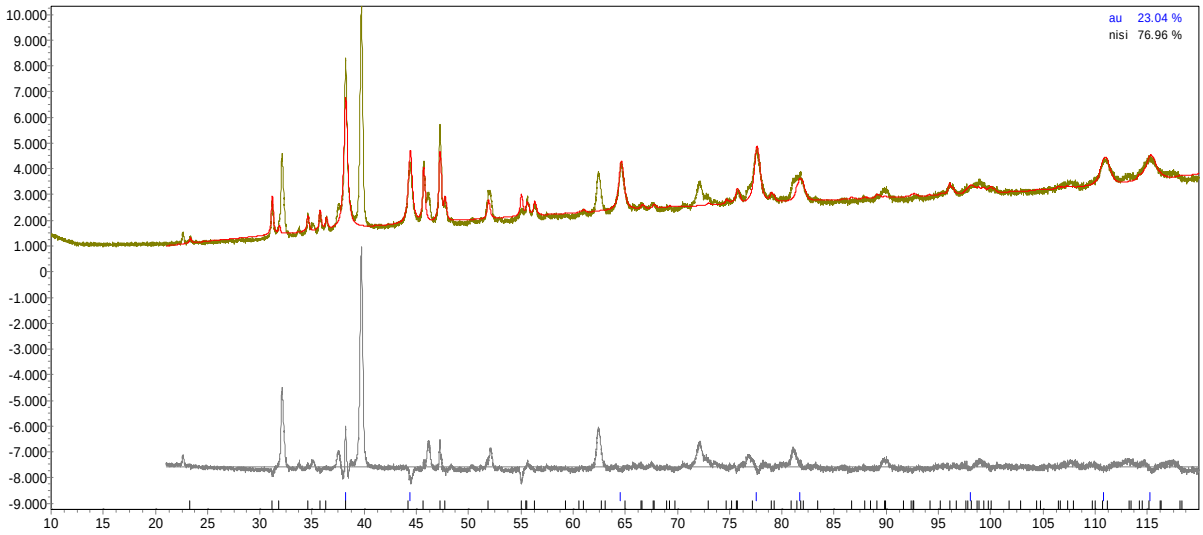

Figure 30: XRD-pattern of B3; green: experiment; red: refinement; grey: difference

The SEM/EPMA results show, that the liquid has partially formed into a metastable phase on quenching. This metastable phase $Au_{17}Si_3$ is mentioned by “Pearson's handbook of crystallographic data for intermetallic phases” [33], but there is no structural information available.

A sample with this composition was prepared, annealed at 500℃ and quenched in water similar to the procedure used for B3 and other samples. Figure 31 presents the XRD-pattern from the metastable phase $Au_{17}Si_3$. This data were used to create a peaks phase in the XRD-refining-software TOPAS. Now the XRD-data together with this peaks-phase were refined and results in an adequate fitting (see Figure 32).

Although no structural information exists about the metastable phase $Au_{17}Si_3$, with this method $Au_{17}Si_3$ was identified in the samples.

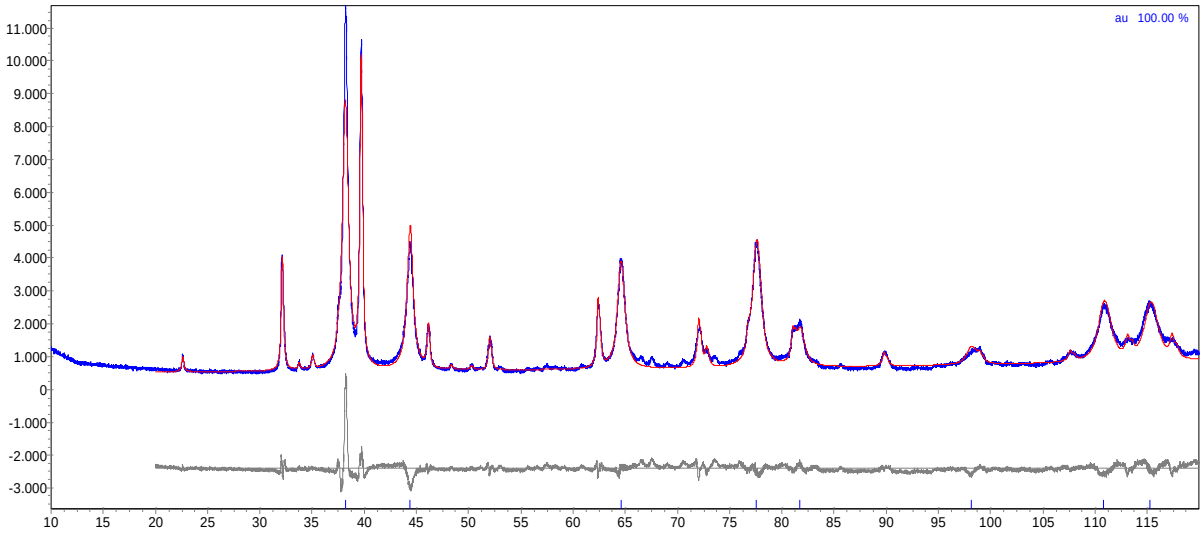

Figure 31: XRD-pattern of A8 with metastable $Au_{17}Si_3$; blue: experiment; red: refinement; grey: difference

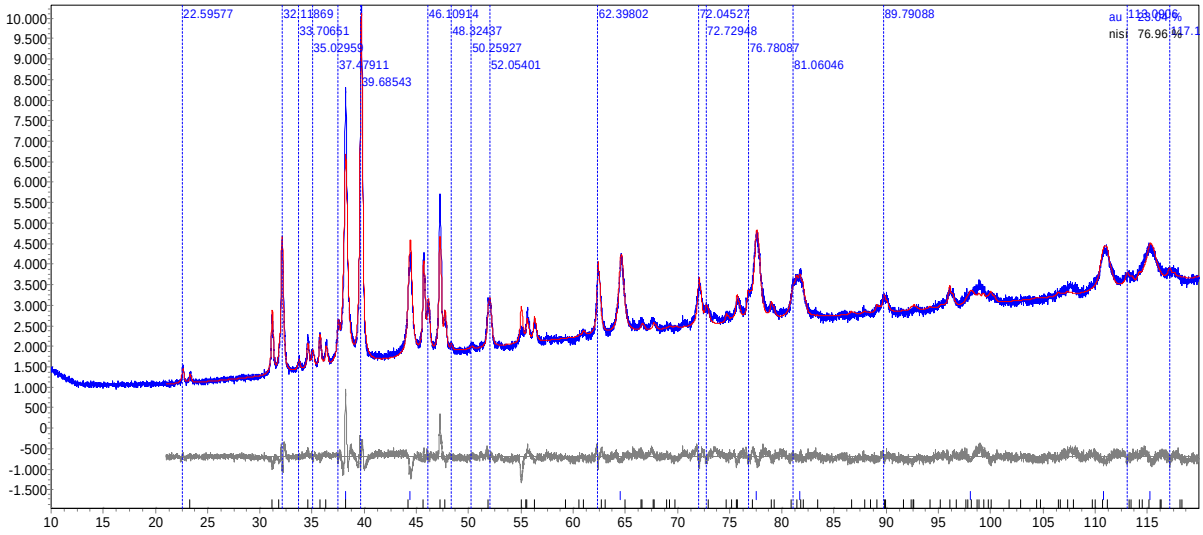

Figure 32: XRD-pattern of B3 with peaks phase of A8; blue: experiment; red: refinement; grey: difference; dashed blue: peaks phase of metastable $Au_{17}Si_3$

5.1.4 Isothermal section at 700℃

Although this isothermal section at 700℃ is more t han 300℃ higher than the binary eutectic temperature, just a small Ni-solubility (0.6 at%) in the liquid phase was observed.

Another interesting detail in this isothermal section is the absence of both ternary phases, which is confirmed by the existence of the 3-phase-field L-Si-$NiSi_2$ (see SEM- and LOM-image of sample D9 in Figure 33). This fact limits the temperature range, where the ternary phases disappear, between 500℃ and 700℃.

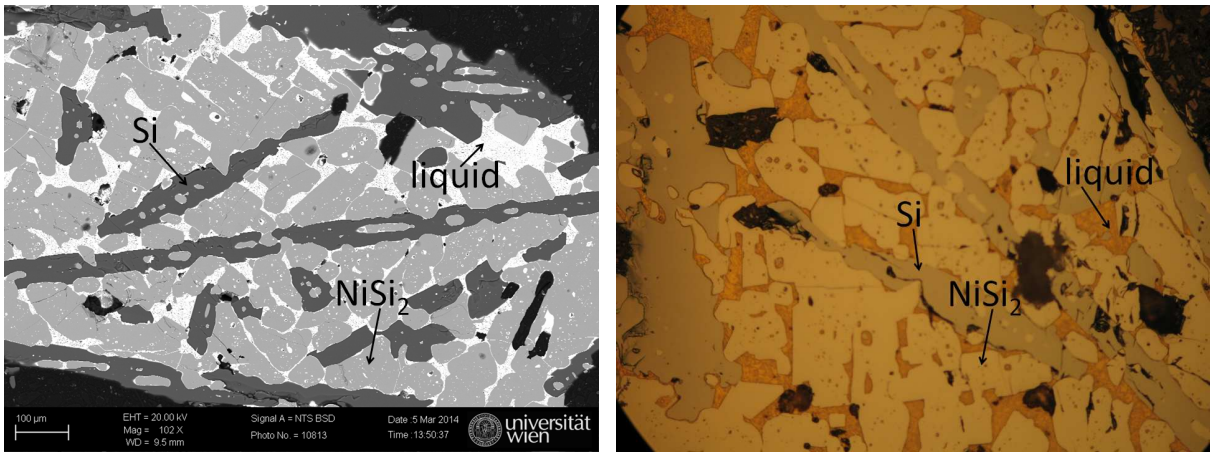

Figure 33: Sample D9 – left: SEM-image, right: LOM-image

Table 10 shows selected data of the phase-composition obtained from the SEM/EPMA-analysis and XRD-analysis.

Figure 34 presents the isothermal section at 700℃. There are seven 3-phase-fields and two 2-phase-fields obtained from the results of the SEM/EPMA-analysis of the samples and another one 3-phase-field which is not confirmed by experiments (dashed line).

Table 10: Experimental data of XRD- & EPMA-analysis at 700℃

nam/annealed composition	**XRD**		**SEM (at%)**		
	phase	lattice parameter	Si	Ni	Au
		Au-Ni_2Si-$Ni_{31}Si_{12}$			
C4 / 700°C Au15Ni60Si25	(Au)	a= 4.073(1)	0.0	12.9	87.1
	Ni_2Si	a= 6.979(1); b= 5.008(1); c=3.719(1)	33.8	66.2	0.0
	$Ni_{31}Si_{12}$	a= 6.676(1); c=12.214(2)	28.8	71.2	0.0
		L-Ni_2Si-Ni_3Si_2			
D8 / 700°C Au10Ni55Si35	L	-	17.6	1.7	80.7
	Ni_2Si	a= 7.180(3); b= 5.096(2); c= 3.710(1)	34.6	65.4	0.0
	Ni_3Si_2	a= 12.343(2); b=10.778(2); c= 6.906(1)	41.0	59.0	0.0
		Au-$Ni_{31}Si_{12}$-Ni_3Si			
C2 / 700°C Au20Ni60Si20	(Au)	a= 4.051(1)	0.0	13.6	86.4
	$Ni_{31}Si_{12}$	a= 6.744(2); c= 12.755(10)	28.3	70.9	0.8
	Ni_3Si	a= 3.515(2)	25.3	74.2	0.5
		L-Ni_3Si_2-NiSi			
D4 / 700°C Au10Ni50Si40	L	-	- [1]	- [1]	- [1]
	Ni_3Si_2	a=12.228(1); b=0.810(1); c=6.924(1)	41.0	58.9	0.1
	NiSi	a= 5.185(1); b=3.335(1); c=5.620(1)	50.9	49.1	0.0

[1] No area scan possible

		Au-Ni-Ni_3Si			
C1 / 700°C Au30Ni60Si10	(Au)	a= 3.994(1)	0.0	29.0	71.0
	Ni	a= 3.527(1)	12.7	86.2	1.1
	Ni_3Si	a= 3.499(1)	25.0	74.7	0.3
D2 / 700°C Au10Ni70Si20	(Au)	a=3.996(1)	0.0	28.7	71.3
	Ni	a= 3.505(1)	13.5	84.7	1.8
	Ni_3Si	a= 3.528(1)	25.4	74.6	0.0
D6 / 700°C Au10Ni75Si15	(Au)	a=3.995(1)	1.4	32.7	65.9
	Ni	a= 3.524(1)	14.7	84.0	1.3
	Ni_3Si	a= 3.517(1)	25.2	74.8	0.0
		L-NiSi-$NiSi_2$			
D5 / 700°C Au10Ni40Si50	L	-	16.1	0.0	83.9
	NiSi	a= 5.184(1); b=3.336(1); c=5.616(1)	50.6	49.4	0.0
	$NiSi_2$	a=5.423(1)	63.7	33.8	2.5
D12 / 700°C Au45Ni15Si40	L	-	20.3	0.6	79.1
	NiSi	a= 5.166(3); b= 3.334(2); c= 5.625(3)	50.6	49.4	0.0
	$NiSi_2$	a= 5.431(1)	63.5	33.9	2.6
		L-$NiSi_2$-Si			
D9 / 700°C Au10Ni23Si67	L	-	25.3	0.6	74.1
	$NiSi_2$	a=5.424(1)	63.5	33.9	2.6
	Si	a=5.431(1)	99.0	0.9	0.1
		Au-Ni			
C5 / 700°C Au37Ni60Si3	(Au)	a= 3.958(1)	0.0	31.4	68.6
	Ni	a= 3.537(1)	6.0	88.9	5.1
D1 / 700°C Au10Ni80Si10	(Au)	a= 3.995(1)	0.0	29.8	70.2
	Ni	a=3.527(1)	11.4	87.0	1.6
		Au-Ni_2Si			
D3 / 700°C Au10Ni60Si30	(Au)	a=4.078(1)	0.0	13.9	86.1
	Ni_2Si	a= 7.060(1); b=5.013(1); c=3.732(1)	34.4	65.6	0.0

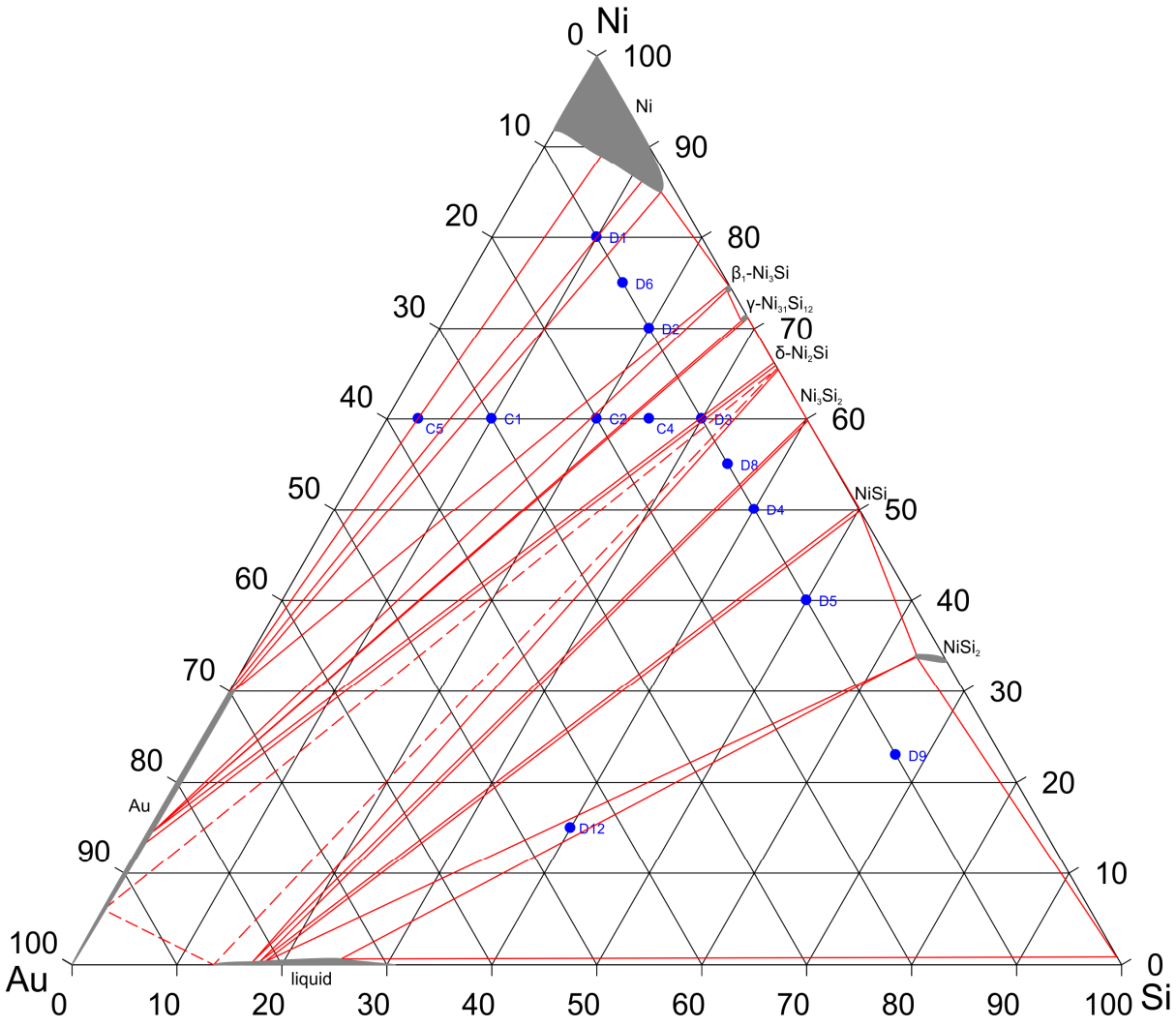

Figure 34: Isothermal section at 700℃; dashed line s are not confirmed by experiments

5.2 The τ_1-Phase $Au_2Ni_4Si_7$

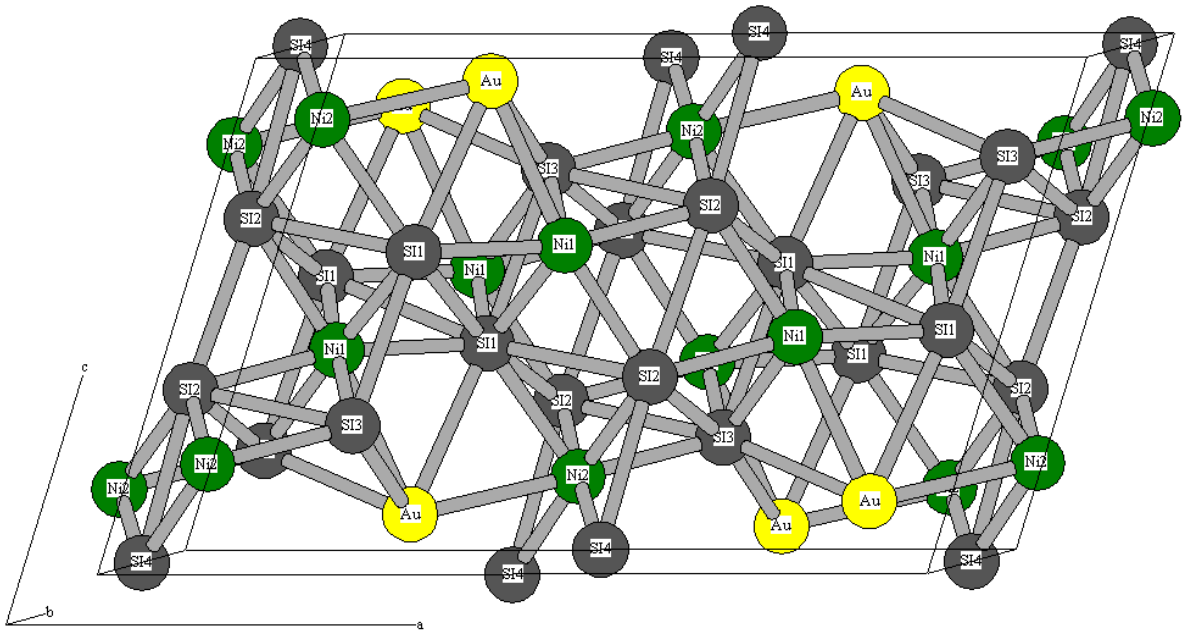

Au2Ni4Si7-Tau1(AuNiSi-1) in C2/m

Figure 35: Unit cell of τ_1

The τ_1-phase was observed at first in small amounts in sample B4 (annealed at 500℃ for 17 days). Further samples (like B7) were prepared to obtain this phase in larger amounts. Composition of τ_1 in these samples varies in following range: Au: 14.5-16.3%; Ni: 31.6-32.1%; Si: 51.9-53.4%.

Sample B7 was used to extract τ_1-crystals (~100-400µm) for structure analysis, see Figure 36 (left: SEM-image, right: similar LOM-image). Some single crystals were prepared and fixed with nail polish on a glass fibre for single crystal-XRD-measurements. Like sample B4, the composition of B7 is close to the 3-phase-region L-τ_1-Si and contains some Si-crystals.

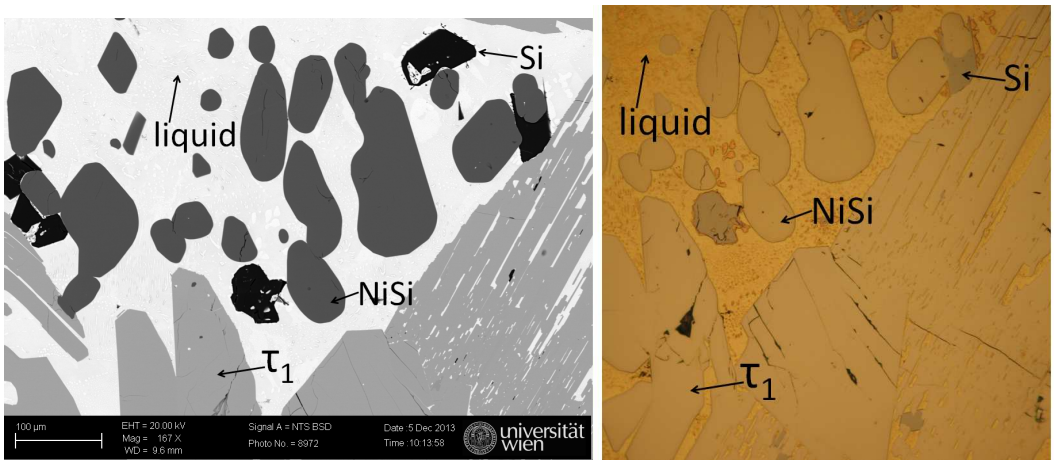

Figure 36: Sample B7- left: SEM-image, right: LOM-image

In the first samples of the A-series no ternary phase τ_1 (or τ_2) could be observed, but the DTA-curves from samples A4-A7 revealed an exothermic peak at temperatures about 480-540℃ (see Figure 37). This is an indicat ion for the metastable state of samples A4-A7 and that a new phase is formed during the exothermic reaction. Figure 37 shows the effect at the first DTA-heating-up-sequence of A5. By forming a new phase the metastable 3-phase-field L-$NiSi_2$-Si converts to a thermodynamically more stable state.

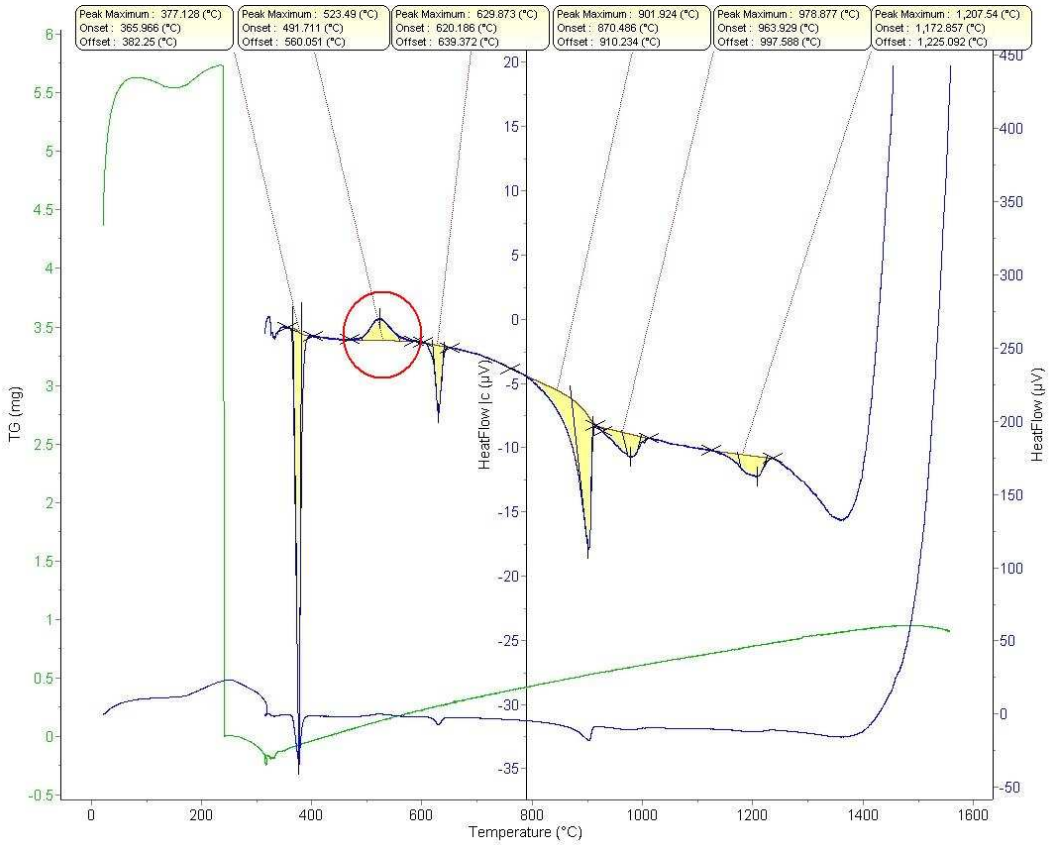

Figure 37: DTA-curve (first heating) of sample A5 = blue curve; red circle: exothermic effect caused by the formation of the ternary phase

According to this, further A-samples were pre-treated at 500℃ and then annealed at 320℃ (see 5.1.1). A pre-treatment at 500℃ for 3 d ays was not enough time for τ_1 to be formed; so 14 days at 500℃ were necessary to en sure the complete formation of τ_1 in the sample.

Figure 38 shows the different 3-phase-fields at 320℃ obtained with a different pre-treatment at 500℃ (Figure 39), whereby only A17 is in equilibrium state (Au-τ_1-Si).

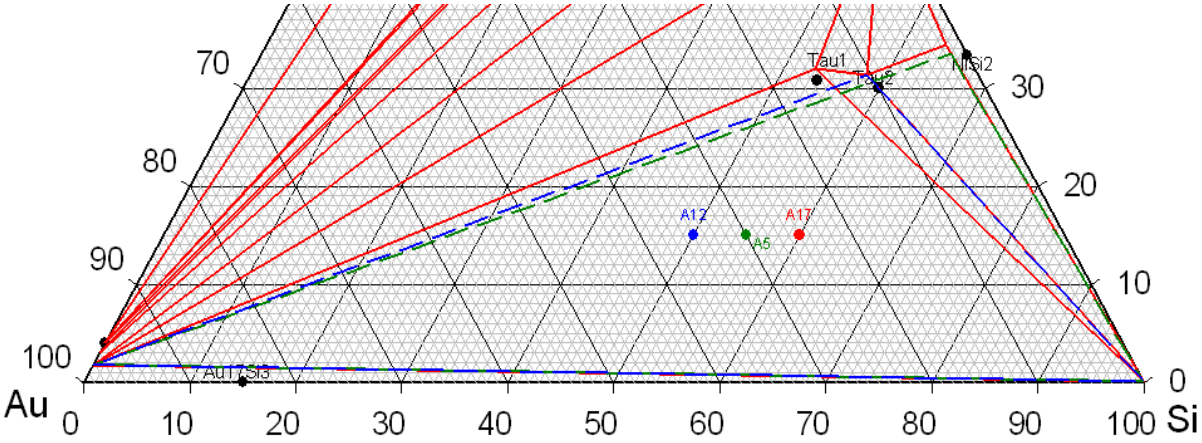

Figure 38: Different phase fields of samples A5, A12, A17

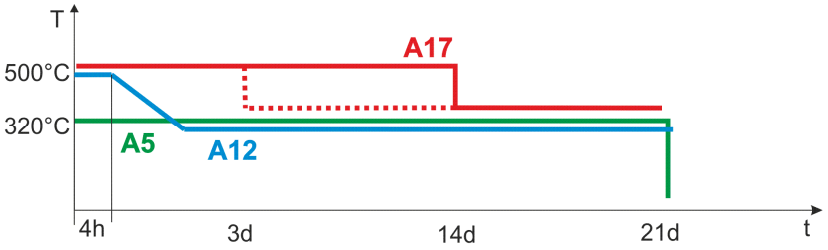

Figure 39: Pre-treatment of samples A5, A12, A17

Above 631℃ τ_1 decomposes by a peritectic reaction into liquid, NiSi and $NiSi_2$ (reaction scheme see the Scheil diagram at Figure 46).

5.2.1 Results of structure determination

Single crystal XRD-measurement and structure analysis was done in collaboration with Prof. Effenberger from the Institute of Mineralogy and Crystallography. By the use of direct methods and subsequent structure refinement the structure parameters could be fully described.

By now there is no isostructural compound reported in literature [44, 45]; τ_1 is a new structure type!

The following tables list the results of the single crystal analysis:

Table 11: Symmetry and unit cell parameters of τ_1

Stoichiometric composition	$Au_2Ni_4Si_7$ (Au15.38Ni30.77Si53.85)
Pearson symbol	mC26
Space group	C 2/m (12)
Lattice parameters	a=12.786 Å b=3.7765 Å c=7.9794 Å β=109.92°

Table 12: Atom positions of τ_1

Atomic site	Multiplicity/ Wyckoff letter	Position x	Position y	Position z	Occupation
Au1:	8j	0.19379	0.0284	0.09281	50%
Ni1:	4i	0.34394	0	0.41091	100%
Ni2:	4i	-0.00554	0	0.83348	100%
Si1:	4i	0.16483	0	0.4233	100%
Si2:	4i	0.49501	0	0.6656	100%
Si3:	4i	0.15479	0	0.7596	100%
Si4:	2b	0	0.5	0	100%

The Au1-atom-position could also be interpreted as a 4-fold-position with 100% occupation. The 8-fold-position fits better at XRD-refinement (lower displacement parameters); the 4-fold-position was used for the graphical structure presentation.

Table 13: Atom positions of τ_1 – Au on the 4-fold-position

Atomic site	Multiplicity/ Wyckoff letter	Position x	Position y	Position z	Occupation
Au1:	4i	0.19379	0	0.09281	100%

This data was used to describe the structure τ_1 for the XRD-refinement; as can be seen in Figure 40 it fits well. The peak at 40° results from the metastable phase $Au_{17}Si_3$, which is formed from the liquid during the quenching process.

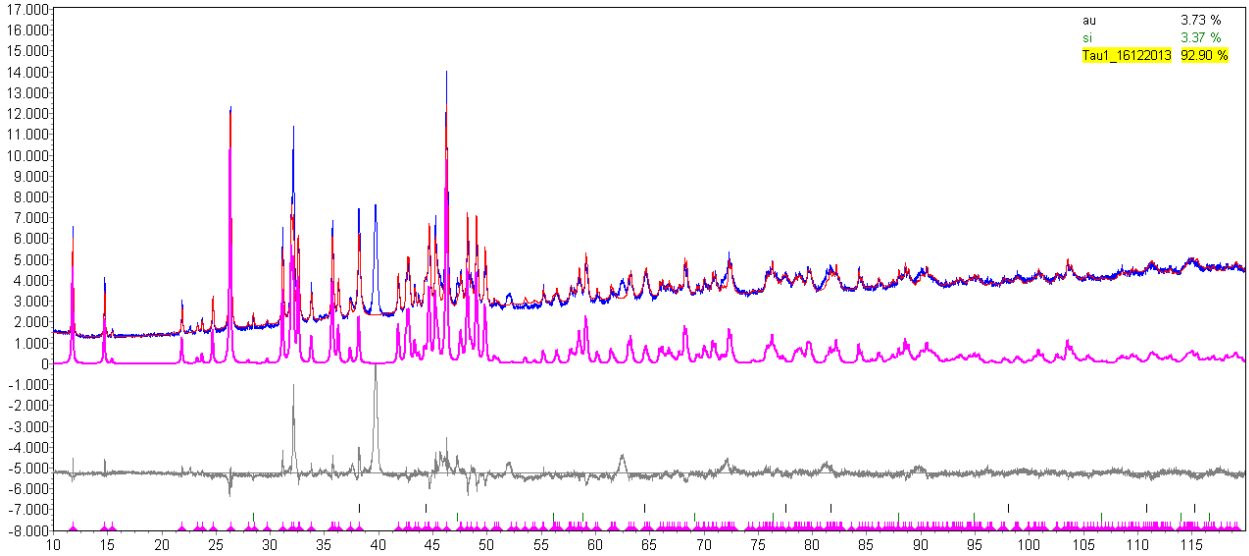

Figure 40: XRD-pattern of B7; blue: experiment; red: refinement; pink: calculated τ_1-pattern, missing lines correspond to $Au_{17}Si_3$ (metastable)

5.2.2 Comparison τ_1 – $NiSi_2$

The composition of the ternary phase τ_1 is not far away from the binary phase $NiSi_2$ (CaF_2-structure); and so structure relation appears possible.

The Ni-atom in $NiSi_2$ is cubic-coordinated by 8 Si-atoms. The coordination number of the Si-atom is 10; it is coordinated by 4 Ni-atoms (tetrahedral) and 6 Si-atoms (octahedral) – see .Figure 41.

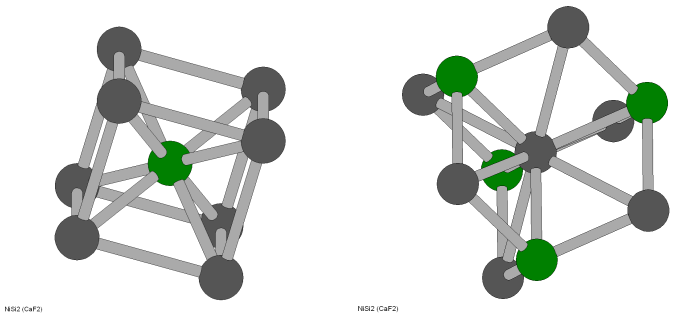

Figure 41: Atom-coordination of $NiSi_2$ – left: Nickel; right: Silicon

Based on the coordination of atoms (see Table 14) there is a partial structural relation between the two structures of τ_1 and $NiSi_2$: Ni1, Si1 and Si2 fully resemble Ni and Si in CaF_2-type $NiSi_2$. Au replaces Si in $NiSi_2$; the coordination is at least partially the same. Si3 and Ni2 are related to Si and Ni (1 Ni-atom is missing at Si3, 1 Ni-atom

is too much at Ni2). The Si4 of τ_1 structure is coordinated by 10 atoms (equal to Si in $NiSi_2$), but the 4 Ni are planar-coordinated instead of tetrahedral.

Table 14: Comparison of τ_1 & $NiSi_2$ (atom-coordination)

τ_1	$NiSi_2$
Ni1: 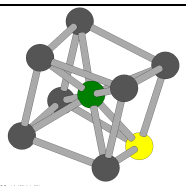	Ni: 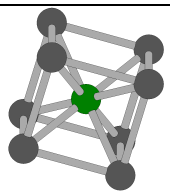
Si1: 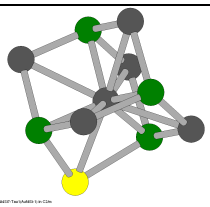 Si2: 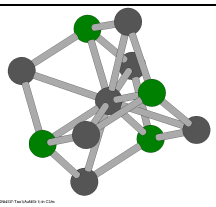	Si: 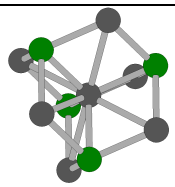
Au1: 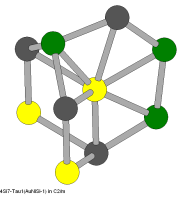	Si: 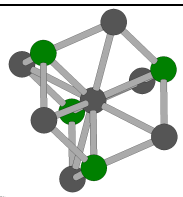
Si3: 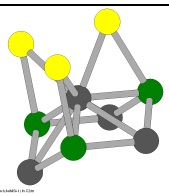	Si: 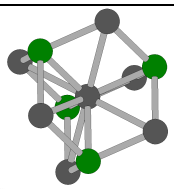
Ni2: 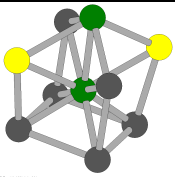	Ni: 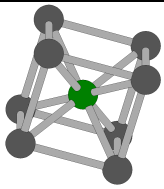
Si4: 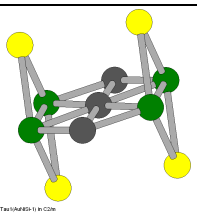	Si: 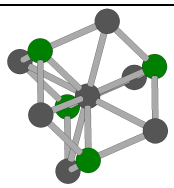

5.3 The τ_2-Phase $AuNi_3Si_6$

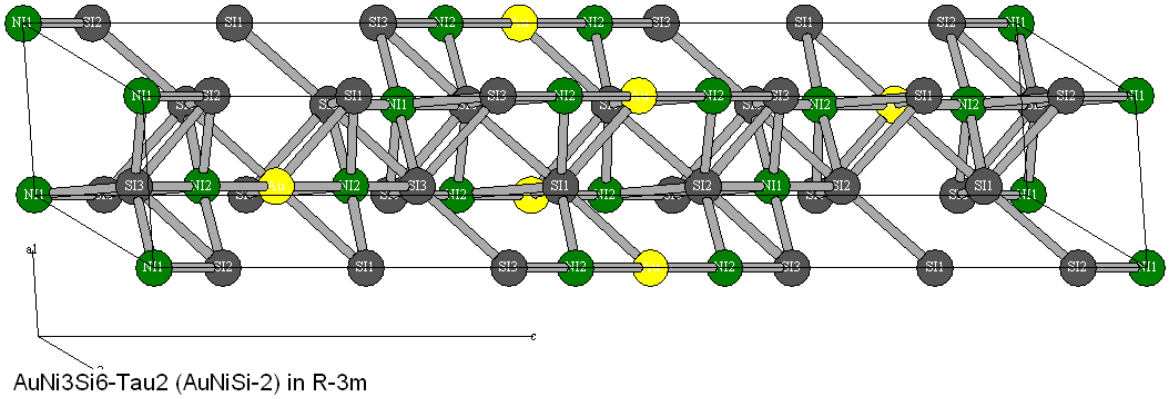

Figure 42: Unit cell of τ_2

The τ_2-phase was the major phase observed in sample B5 (annealed at 500℃ for 17 days). The sample B5 includes three phases: τ_2 (majority), τ_1 (minority) and $NiSi_2$ in small amounts; see SEM-image in Figure 43.

Samples with the same composition as τ_2 supplied no suitable single crystals. It was later found out, that τ_2 does not crystallize from the melt. So the sample B5 was used to obtain adequate single-crystals for structure analysis – with success!

Further samples were prepared showing τ_2 in equilibrium with different phases; the composition varies in following range: Au: 14.5-16.3%; Ni: 31.6-32.1%; Si: 51.9-53.4%.

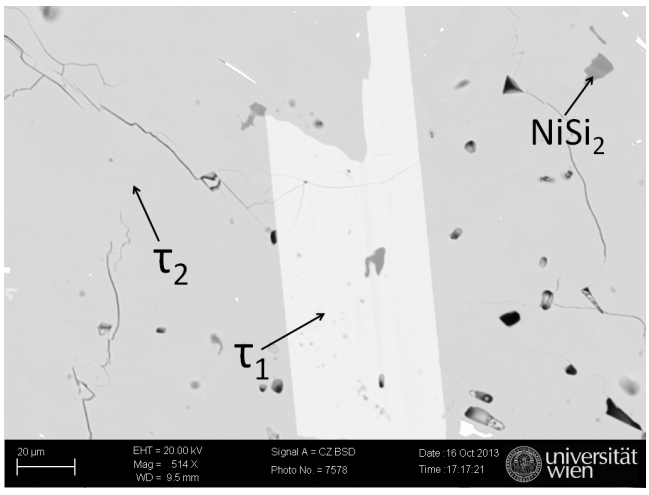

Figure 43: SEM-image of sample B5

As described before, no ternary phase was observed in samples directly annealed at 320℃. In contrast to the difficult formation of τ_1, a pre-treatment of 4h at 500℃ was sufficient to convert the metastable equilibrium completely to τ_2.

Above 608℃ τ_2 decomposes in a peritectoidic reaction into τ_1, Si and $NiSi_2$ (reaction scheme see Figure 46). τ_2 decomposes before τ_1, but for kinetic reasons it is the first phase formed at 500℃ in the solid state.

5.3.1 Results of structure determination

Single crystal XRD-measurement and structure analysis was again done by Prof. Effenberger from the institute of mineralogy and crystallography.

Like τ_1, there was no isostructural component reported to τ_2 in literature [44, 45]; so it is a new structure type!

The following tables list the results of the single crystal analysis:

Table 15: Symmetry and unit cell parameters of τ_2

Stoichiometric composition	$AuNi_3Si_6$ (Au10Ni30Si60)
Pearson symbol	hR30
Space group	R $\bar{3}$ 2/m (166)
Lattice parameters	a=3,769 Å c=33,87 Å

Table 16: Atom positions of τ_2

Atomic site	Multiplicity/ Wyckoff letter	Position x	Position y	Position z	Occupation
Au1:	3b	0	0	0.5	100%
Ni1:	3a	0	0	0	100%
Ni2:	6c	0	0	0.42513	100%
Si1:	6c	0	0	0.78685	100%
Si2:	6c	0	0	0.06983	100%
Si3:	6c	0	0	0.64238	100%

This data was used to for powder-XRD-refinement; as can be seen in Figure 44 it fits well.

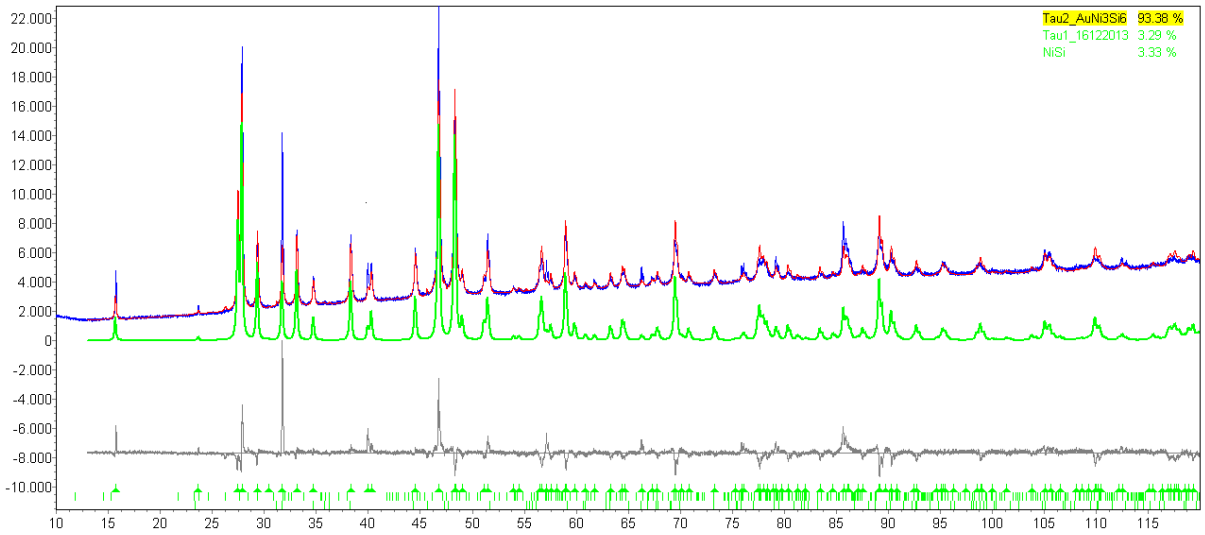

Figure 44: X-ray-diffractogram of B5; blue: experiment; red: refinement; green: calculated τ_2-pattern

5.3.2 Comparison τ_2 – $NiSi_2$

The comparison between τ_2 and $NiSi_2$ reveals a close structural relation. As can be seen in Figure 45 (polyhedral view), the τ_2 structure can be interpreted as a distorted $NiSi_2$-structure, which is interrupted by a gold layer. In the $NiSi_2$-structure there are NiSi-cubes (Si in the corner, Ni in central position), which are connected by the edge like a 3-dimensional chess table. The τ_2-structure introduces a gold layer between every third NiSi-cube, whereby the Au-atom substitutes one Si-atom in the $NiSi_2$-corner. Divided by this gold layer, the NiSi-cubes are now connected by the corner (Au-atom).

Also, the comparison of the coordination spheres between the ternary and the binary structure (see Table 17) shows a definite agreement, except for the Au-atom, which has only 2 instead of 4 Ni neighbours.

The Si1 atom of τ_2 corresponds to the Si3 atom of τ_1 (same coordination environment).

τ_2	$NiSi_2$
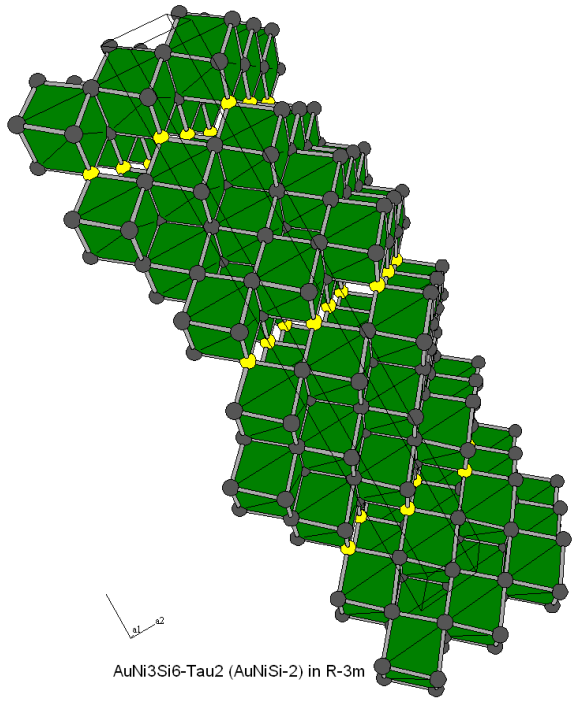	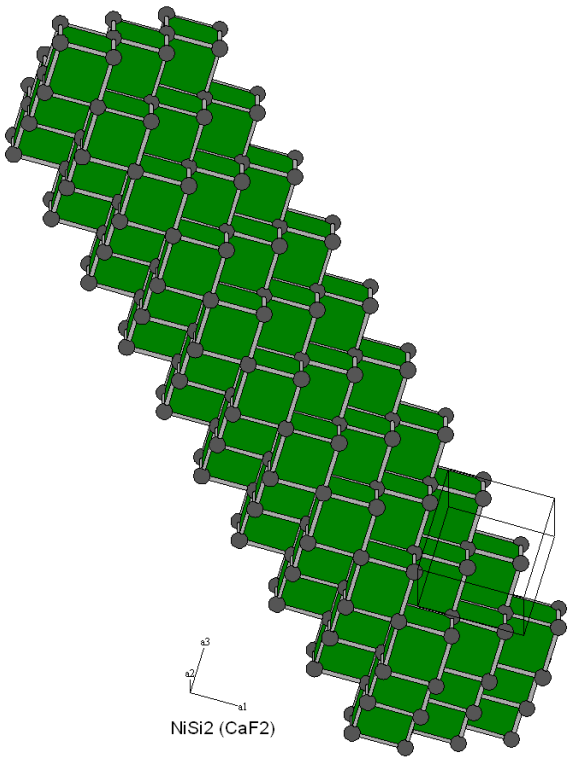

Figure 45: Comparison of τ_2 & $NiSi_2$ (polyhedral view)

Table 17: Comparison of τ_2 & $NiSi_2$ (atom-coordination)

τ_2	$NiSi_2$
Ni1: 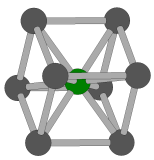 Ni2: 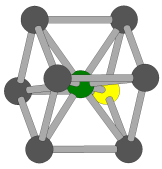	Ni: 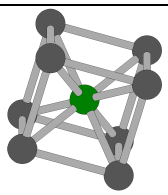
Si2: 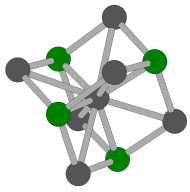 Si3: 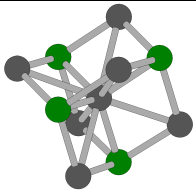	Si: 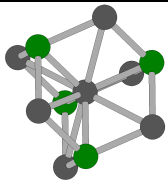
Au1: 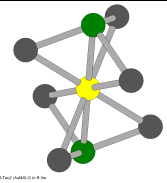	Si: 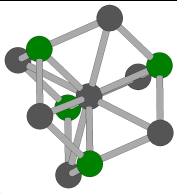
Si1: 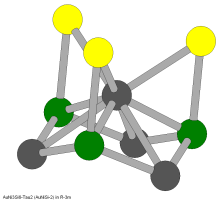	Si: 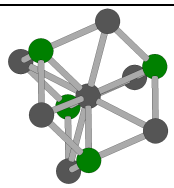

5.4 Scheil diagram (reaction scheme)

The reaction scheme is an important tool for understanding the processes which occur during heating or cooling the alloy.

To reveal the reaction scheme, a sequence of reactions must be found, which brings all data into accordance. This was done in an iterative way by combining DTA results with the information of isothermal sections and binary systems.

The data of thermal analysis yield the reaction temperature. The peaks of the DTA-measurements were analysed and it was tried, to assign every peak to a reaction type (invariant, non-invariant). The presented reaction temperatures in the reaction scheme illustrate the averaged and rounded values.

To explore the reactions involving the ternary phases, the isothermal sections up to 700℃ were helpful. One of the results was, that τ_2 decomposes at 608℃ and τ_1 at 631℃ in a peritectic reaction. Around this tempera ture the liquid phase starts to extend more into the ternary phase diagram.

Assuming the absence of any further ternary phase, the DTA-data were used to investigate the complete reaction scheme up to the liquidus line, although there are no more isothermal sections available.

Matters were complicated by the circumstance, that the phase equilibria involving Au+Ni+β_1 were hard to analyse by thermal analysis. It is obvious from the binary Au-Ni-phase diagram (compare Figure 14), that the phase boundaries change dramatically between ~800℃ and the liquidus line.

It is assumed that during DTA-measurements with a heating rate about 5K/min there is no chance to equilibrate these states, especially if there are only solid phases present.

So it can be assumed, that thermal analysis does not always display all effects, which should occur in samples according to the reaction scheme.

It is inevitable to make further experiments with samples annealed above 700℃. So the ternary phase diagram could be exactly explored at higher temperatures.

Anyway, a Scheil diagram was constructed, which meets all conditions for constructing reactions schemes/phase diagrams and is widely consistent with the collected data.

Figure 46 represents the reaction scheme, which was done by my best knowledge. It is in good agreement with all effects observed on thermal analysis and isothermal

sections. Reactions which are not proved by isothermal sections are presented with dashed lines.

Except reaction U9, every invariant reaction was assigned with invariant peaks from thermal analysis and so the reaction temperature was determined.

Reaction U9 (L+β_2-Ni_3Si ⇌ Au/Ni+ γ) must occur between 1024℃ and 1143℃ and was not found in the present study, because all sample-compositions are outside from the primary crystallization field of β_2-Ni_3Si.

Finally it should be noted, that the predicted reactions from [42], where the invariant reactions L ⇌ Au+Ni+ β_1-Ni_3Si and L+$Ni_{31}Si_{12}$ ⇌ Au+ β_1-Ni_3Si are proposed, was not found in the reaction scheme. This way would lead to a reaction, where the liquid disappears by heating (β_1 ends in the binary Ni-Si without any liquid phase). Although this reaction type is possible, it is very unlikely und was discarded.

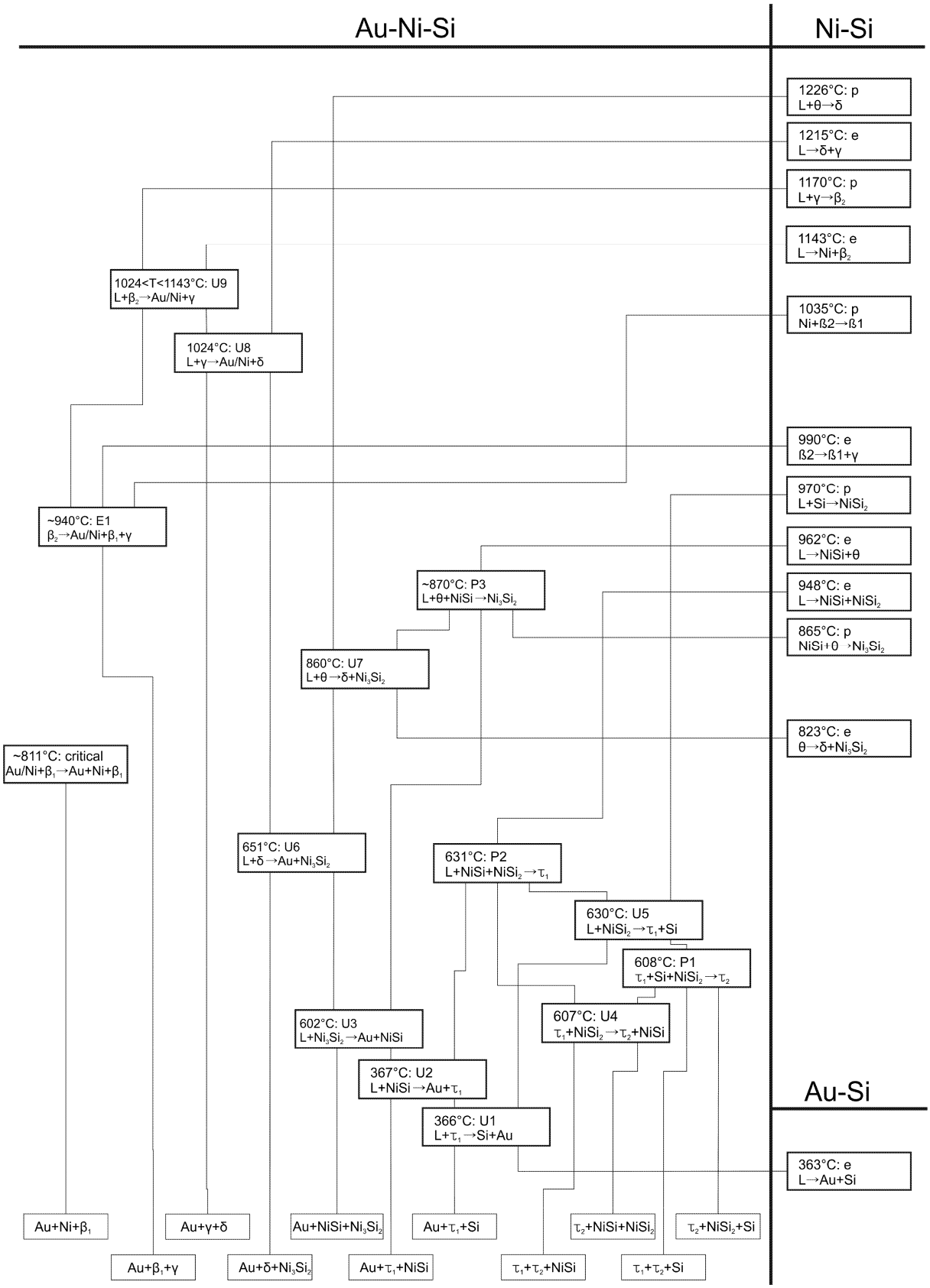

Figure 46: Scheil diagram (reaction scheme) of Au-Ni-Si system

5.5 Isopleths

The data of the thermal analysis, the isothermal sections and the reaction scheme were combined to the following four isopleths: 15at% Ni, 30at% Ni, 60at% Ni and 10at% Au. Up to 700℃ the vertical sections are wel l founded because they are also consistent with the isothermal sections; above 700°C only the existing data of the thermal analysis could be used to construct the vertical sections.

In an iterative process the isopleths together with the reaction scheme and the liquidus surface projection were constructed until all existing data fit together. Because the data of isothermal sections are limited with 700℃, the speculative part of the isopleths is illustrated with dashed lines.

5.5.1 Isopleth 10 at.% Au

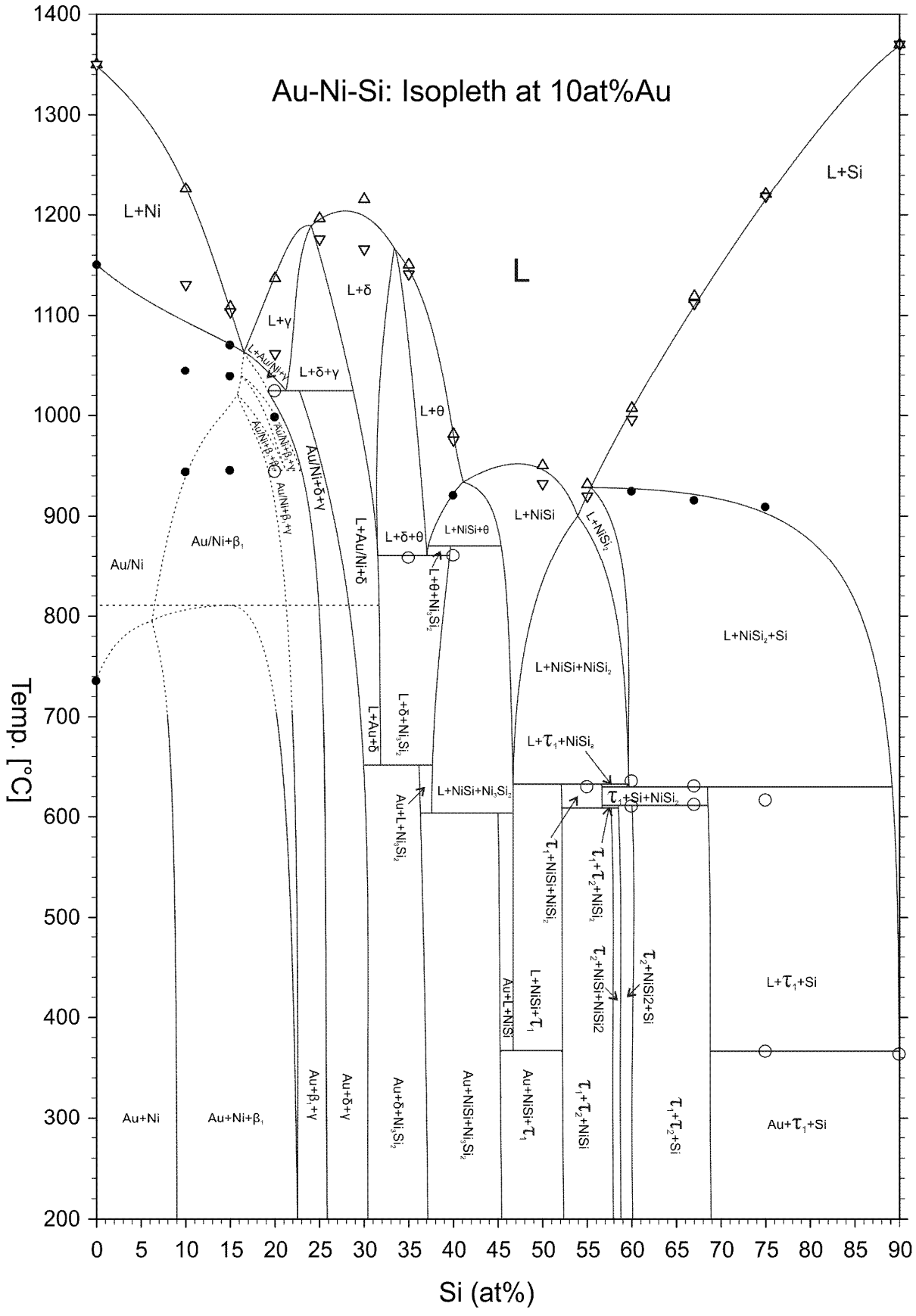

Figure 47: Isopleth of Au-Ni-Si system at 10at% gold

5.5.2 Isopleth 15 at.% Ni

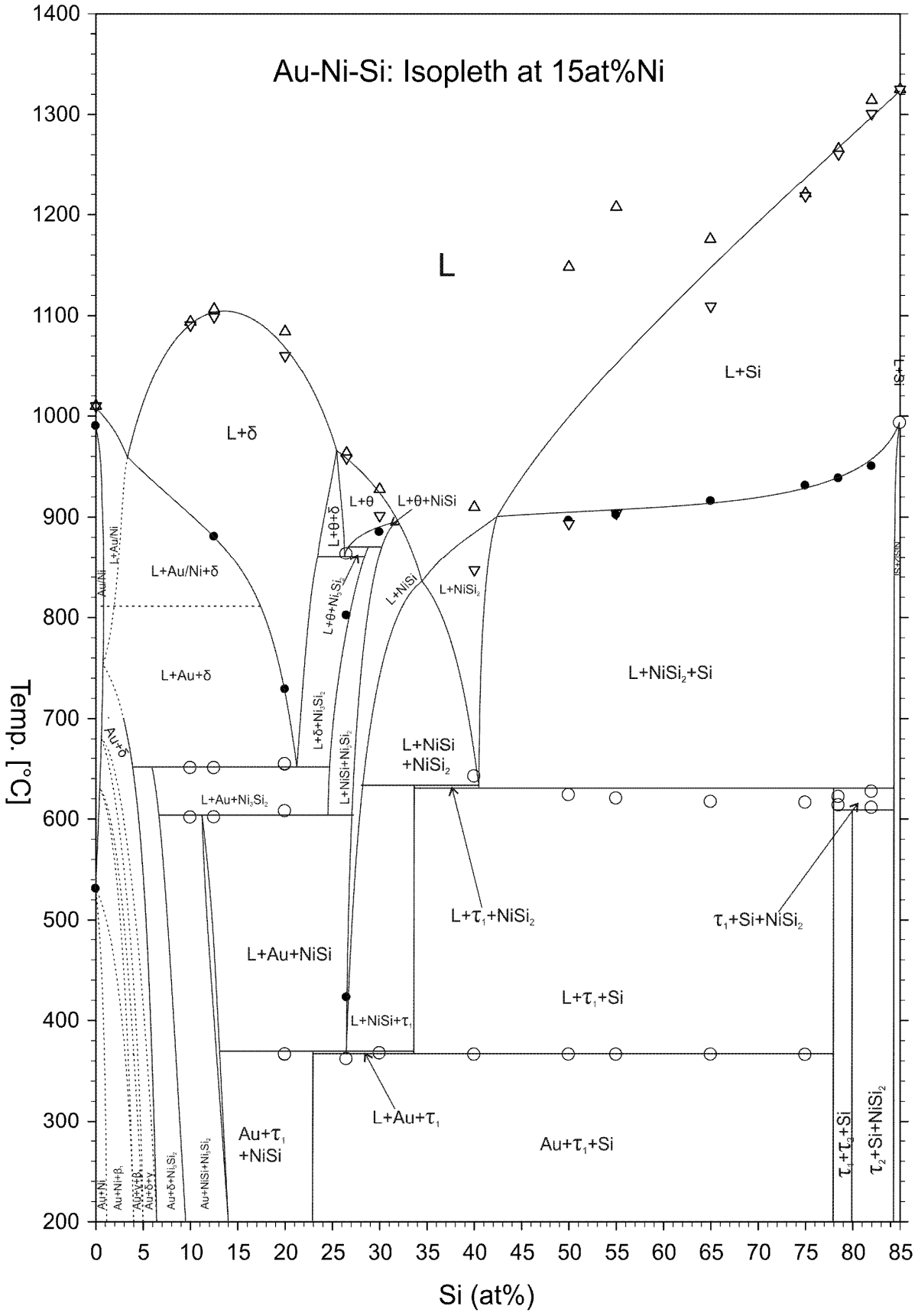

Figure 48: Isopleth of Au-Ni-Si system at 15at% nickel

5.5.3 Isopleth 30 at.% Ni

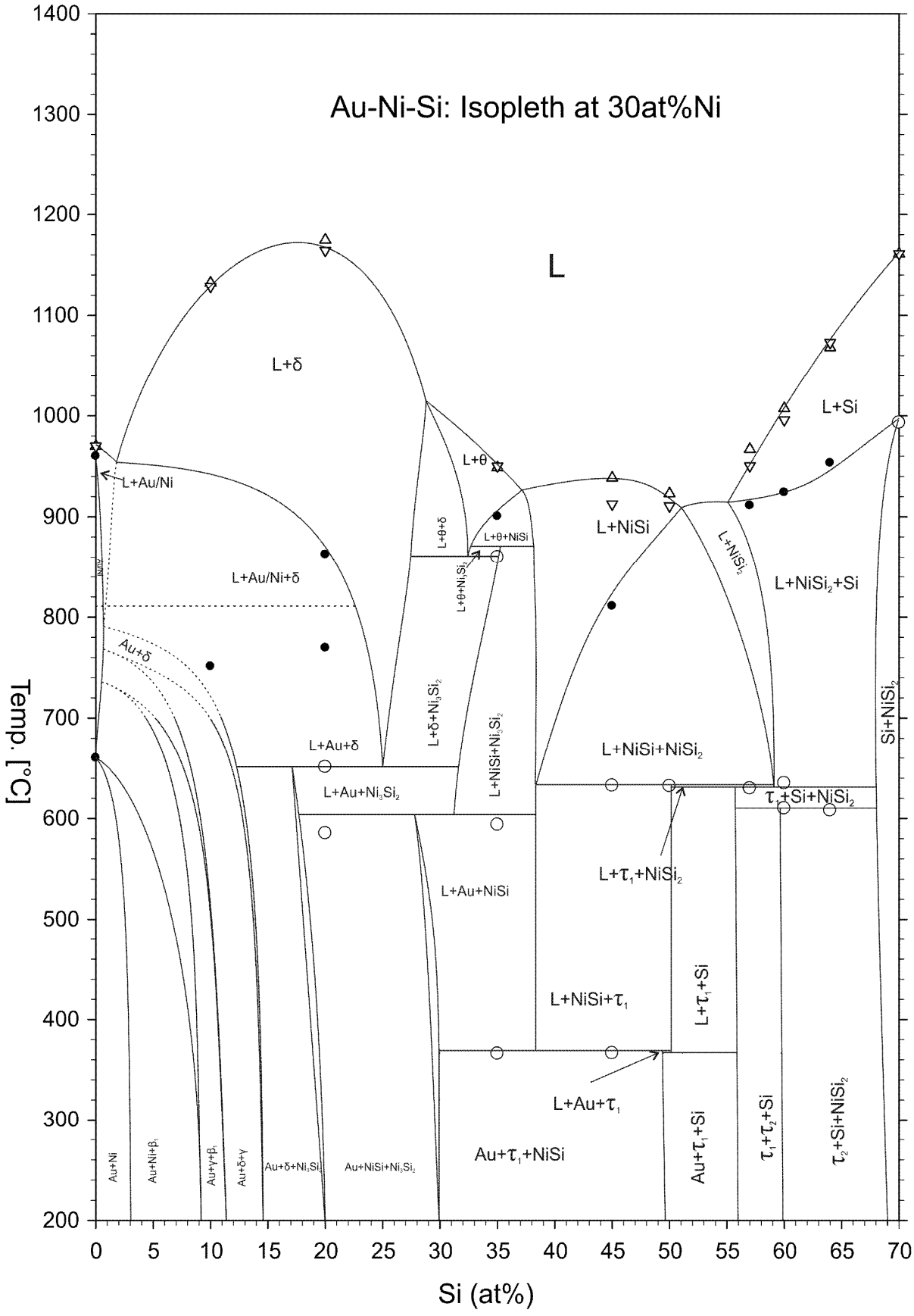

Figure 49: Isopleth of Au-Ni-Si system at 30at% nickel

5.5.4 Isopleth 60 at.% Ni

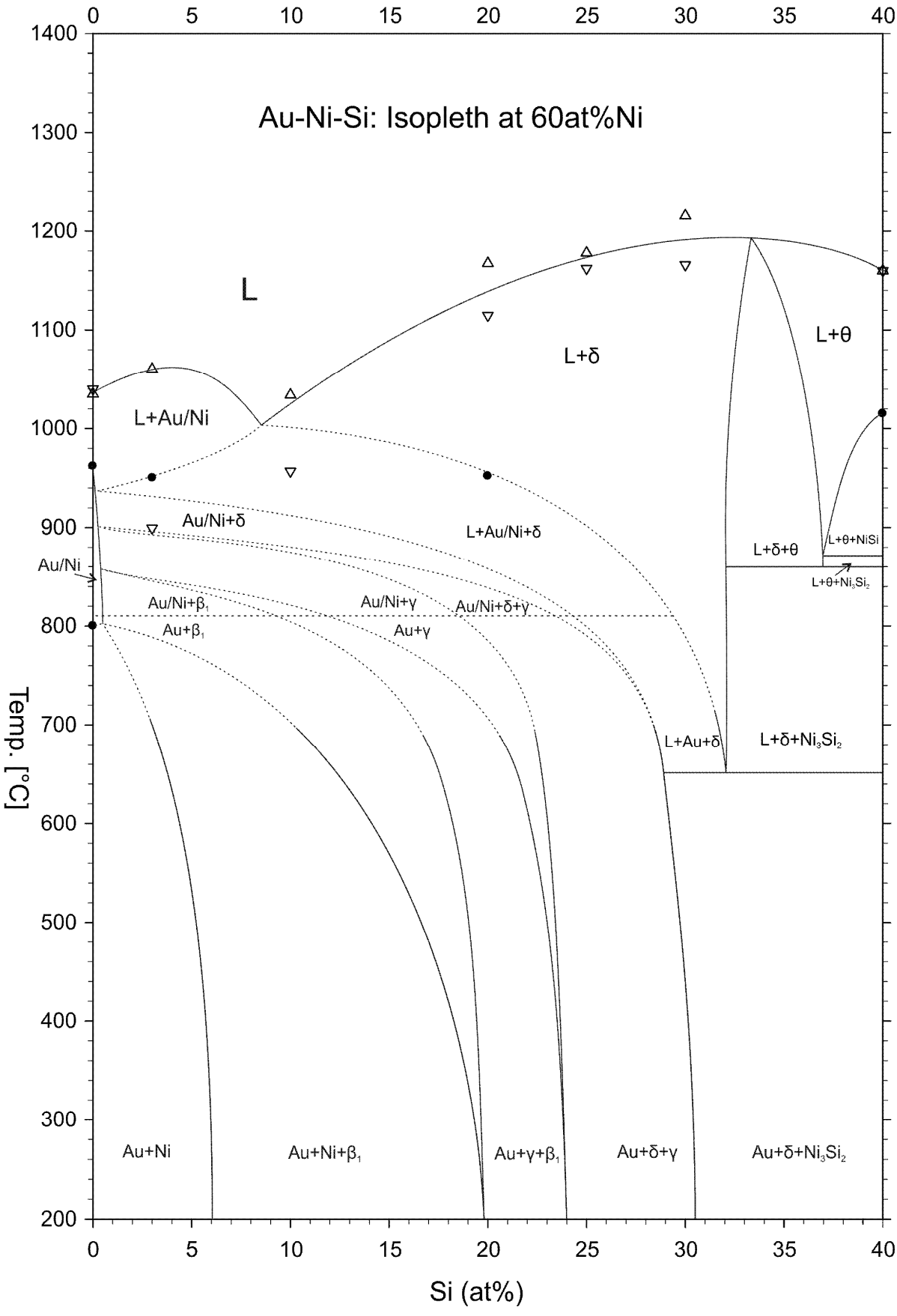

Figure 50: Isopleth of Au-Ni-Si system at 60at% nickel

5.6 Liquidus surface projection

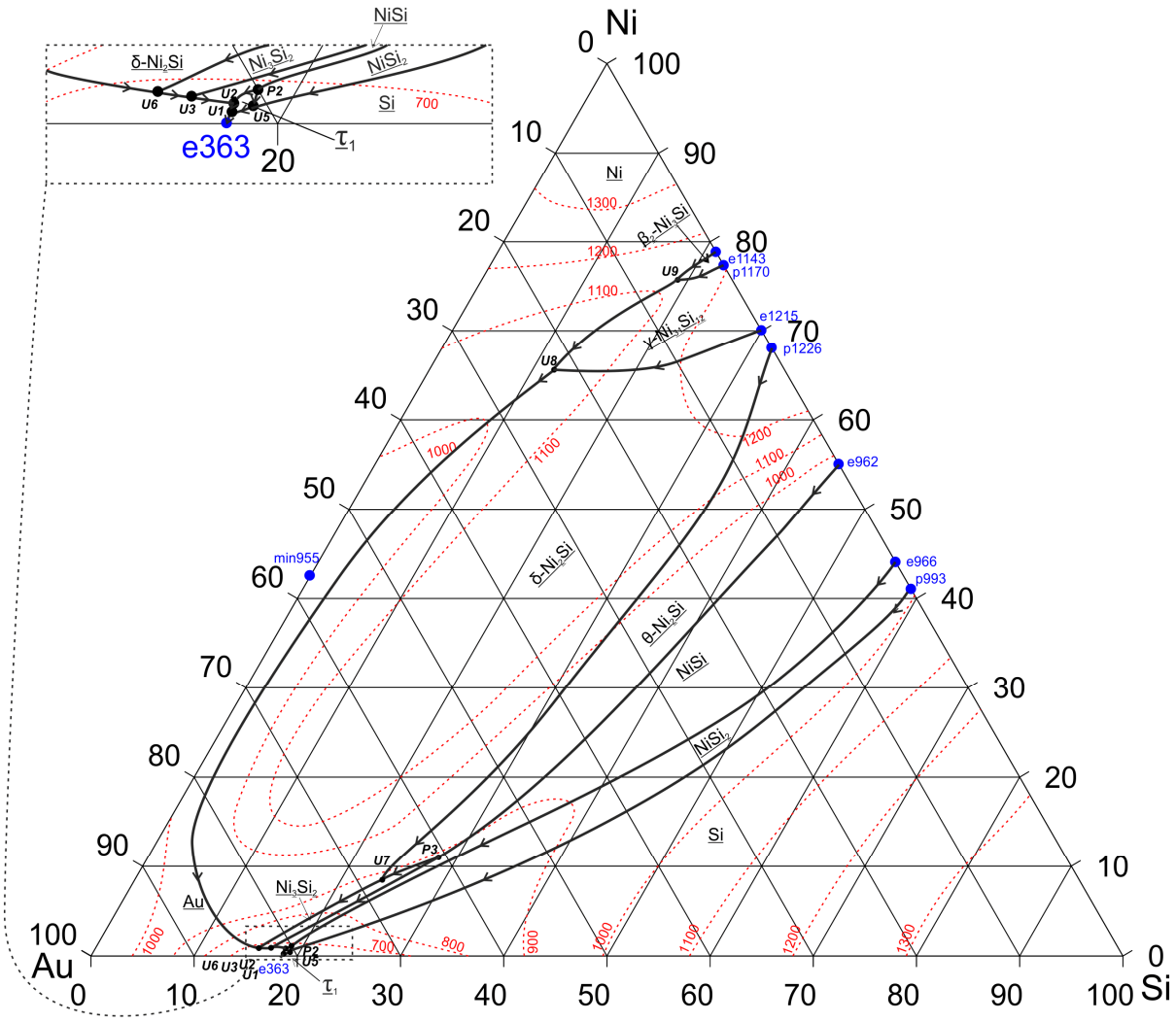

Figure 51: Liquidus surface projection of Au-Ni-Si system

As described before, the liquidus surface projection was constructed together with the other graphs in an iterative way. It shows the liquidus lines, the isothermal lines (lines with the same melting temperature) and gives information about the primary crystallization fields.

As observed at the SEM/EPMA-results there is only a small Ni-solubility in the liquid phase at 700℃. Samples with 4at% Ni were prepared to prove this. The thermal analysis of the samples A18, A19 and A20 yields melting points above 750℃ and confirms this remarkable behavior.

The isothermal lines near to the binary eutectic are close together up to 700℃, so the liquidus line rises up sharply to higher temperatures in this region.

Starting from the binary Au-Si-eutectic point, the liquid phase begins to enter the ternary system. The liquid-temperature rises sharply up to 700℃ and then nickel starts to be dissolved in the liquid.
The binary phase δ-$NiSi_2$ shows an extended primary crystallization. In contrast, the primary crystallization field of Ni_3Si_2 and τ_1 is very small (see the zoomed region in Figure 51).

5.7 Wetting experiments

The deep eutectic temperature (363℃) of the binary Au-Si system makes it attractive for soldering and brazing applications. As nickel is often used as metallization layer in electronics, the wetting behaviour of Au-Si-eutectic with Ni is of interest. In a previous work by Amir Blazevic (Phase equilibria and structural investigations in the ternary system Au-Cu-Si)[46] the wetting angle of the Au-Si-eutectic on a copper-plate was investigated and no wetting was observed at different temperatures.
Now comparable wetting experiments were done on a nickel plate (diameter 16mm), which was freshly polished with Al2O3 (1µm) and cleaned with acetone and distilled water. A pill with the exact Au-Si eutectic (Au81.4Si18.6) composition was prepared using arc melting. This pill was used as cast and a piece of it was analysed by thermal analysis. The DTA-data results a melting temperature of 366,2° and considering the measurement accuracy it corresponds to the binary eutectic melting temperature. This confirms the eutectic composition of the prepared sample.
A piece of this pill was placed on the nickel plate (see Figure 52) and placed into a furnace, which was evacuated and flushed with argon (99.999%) three times. Afterwards under constant argon gas flow (40ml/min) the furnace was heated. A temperature program according to Figure 55 was used to perform the wetting experiment at 385℃. During the experiment a CCD-ca mera records pictures of the Au-Si-piece on the nickel plate to analyse the wetting angle (see Figure 53 and Figure 54). Although the Au-Si-piece melted (it deformed slightly), no wetting on the nickel plate was observed. There was also no adhesion of the Au-Si-droplet on the nickel plate. A possible reason is an oxide-layer, which keeps this droplet in shape and prevents wetting.

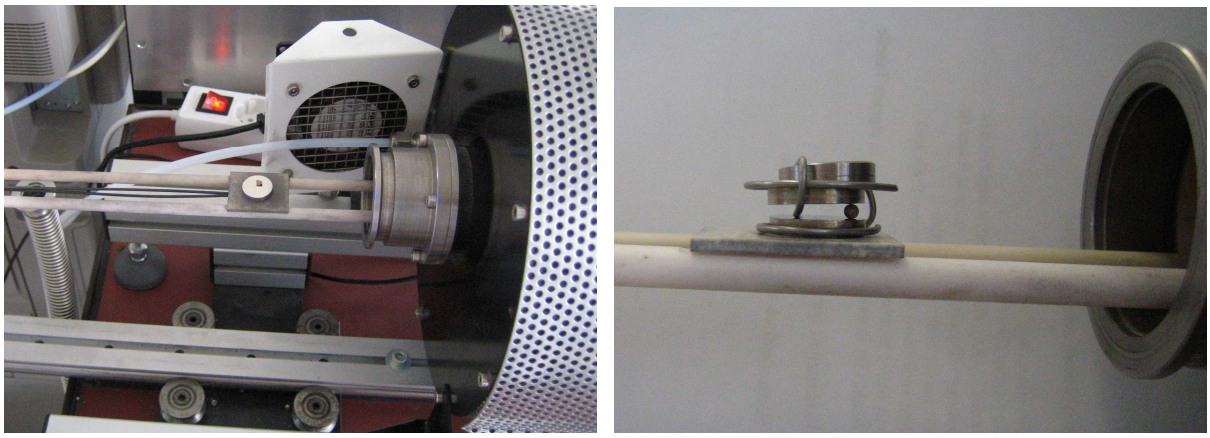

Figure 52: Positioning of the Au-Si-piece on the nickel plate – left: without ballast; right: two nickel plates act as a ballast

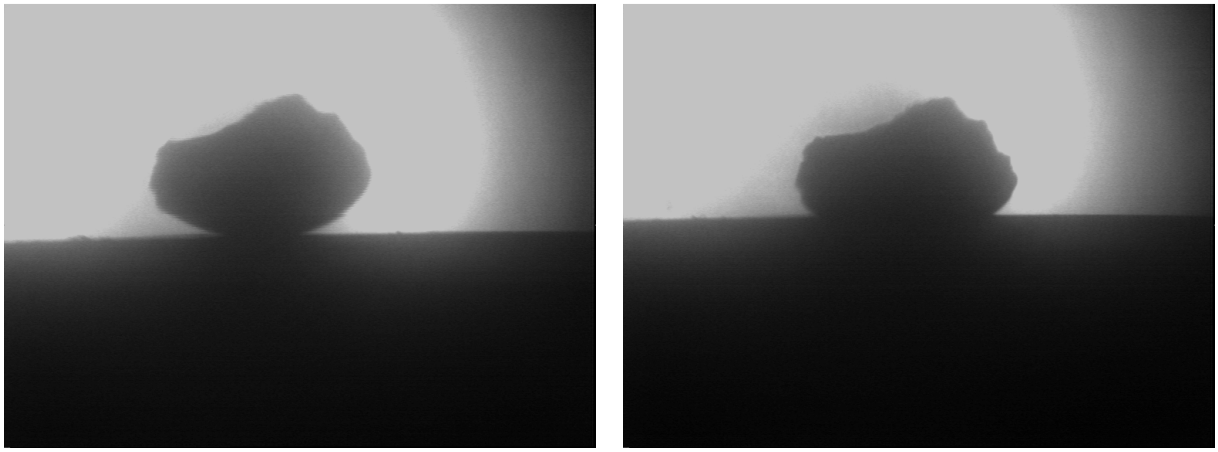

Figure 53: Piece of Au-Si on nickel plate – left: before heating; right: after heating

Another wetting experiment was performed with the approach to solve the problem regarding the oxide layer. Two nickel plates were placed additionally on the top of the Au-Si-piece (see Figure 52) and then the experiment was started. The two plates put pressure on the Au-Si-droplet and were meant to burst the potential oxide layer. The experimental conditions were like in the first experiment, but the furnace was now heated up to 395℃. During the experiment the Au-Si -piece shifted slightly out of position. Although the resulting Au-Si-droplet was pressed flat, again no wetting was observed (see Figure 54). The results of the wetting experiments with Au-Si on the nickel plate are thus disappointing.

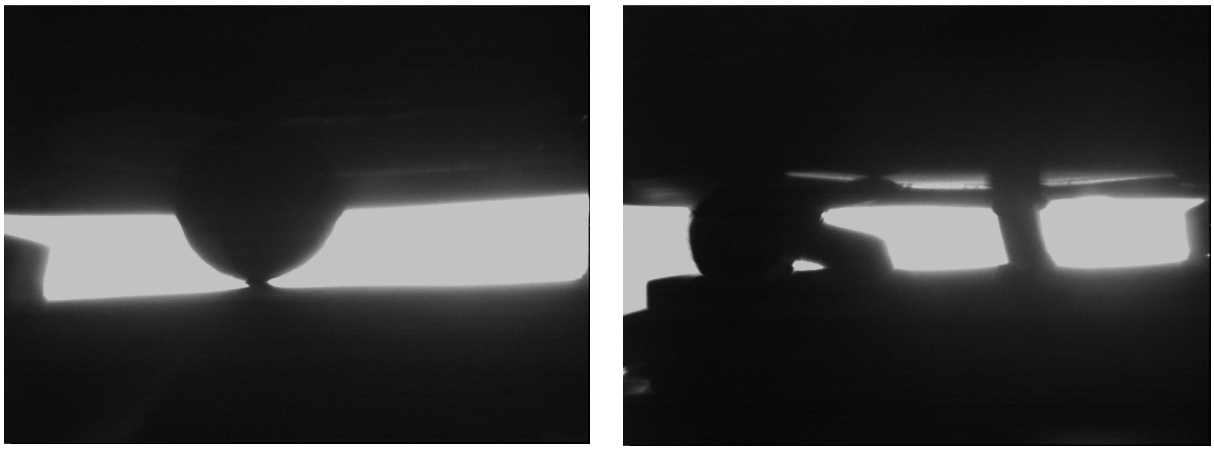

Figure 54: Wetting experiment with two nickel plates as ballast – left: before heating; right: after heating (Au-Si piece shifted away)

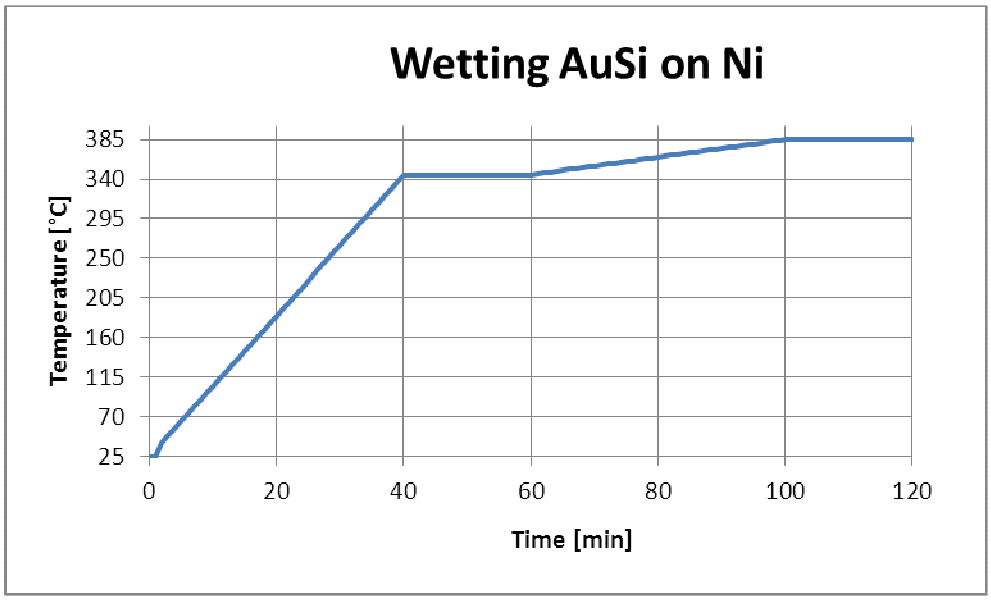

Figure 55: Temperature program for wetting experiment

6 Abstract

The deep eutectic point (363℃) of the binary system Au-Si-system makes it attractive as a possible material for joining applications. Nickel is often used for metallization layers in electronics and so the interactions of Au-Si with Ni are of interest.

Within this master thesis the ternary system Au-Ni-Si was studied in the full composition range by a combination of X-ray diffraction, optical microscopy, scanning electron microscopy and differential thermal analysis.

Isothermal sections at 320℃, 500℃ and 700℃ were constructed and two ternary compounds, τ_1 ($Au_2Ni_4Si_7$, C2/m, mC26) and τ_2 ($AuNi_3Si_6$, $R\bar{3}$ /m, hR30) were identified at compositions close to the binary phase $NiSi_2$. Their crystal structures were investigated by single crystal XRD; both compounds are crystallizing in a new structure type. The structures of τ_1 and τ_2 are closely related to $NiSi_2$ (CaF_2-structure), especially for τ_2 these relations are easy to visualize. The phase τ_1 is formed at 631℃ in a peritectic reaction, τ_2 at 608℃ in a peritectoid reaction.

A complete Scheil diagram, a liquidus surface projection and four vertical sections (10at% Au; 15, 30, 60 at% Ni) were constructed based on DTA results. The identification of phase reactions is well founded up to 700℃, based on the isothermal sections. Some of the phase reactions proposed above 700℃ are speculative due to the lack of reliable data.

Finally, wetting experiments were performed to investigate the wetting of the Au-Si-eutectic composition on a nickel plate. No significant wetting was observed, which corresponds to equal experiments on a copper plate.

Further experiments are necessary confirm the proposed reaction scheme at higher temperature. Therefore it is suggested to investigate isothermal sections above 700℃ (e.g. 900℃). Especially in the Si-poor region, more data are needed which help to clarify the reaction scheme.

7 Zusammenfassung

Das binäre System Au-Si weist einen außerordentlich tiefen eutektischen Punkt (363℃) auf und die eutektische Zusammensetzung kom mt daher als mögliches Löt-Material infrage. In der Elektronik wird Nickel oft zum Metallisieren genützt, daher ist das Reaktionsverhalten von Nickel mit den binären Au-Si Legierungen interessant.
Im Rahmen dieser Master-Arbeit wurde das ternäre System Au-Ni-Si im gesamten Konzentrationsbereich mit den Methoden der Metallographie, Elektronenmikroskopie, Röntgendiffraktometrie sowie mit Differenzthermoanalyse untersucht.
Es wurden isotherme Schitte bei 320℃, 500℃ und 70 0℃ erstellt und dabei wurden zwei ternäre Verbindungen, τ_1 ($Au_2Ni_4Si_7$, C2/m, mC26) und τ_2 ($AuNi_3Si_6$, $R\bar{3}$ /m, hR30), gefunden. Die Zusammensetzung der ternären Phasen liegt nahe bei der binären Phase $NiSi_2$. Beide Strukturen wurden mit Hilfe der Einkristall-Röntgendiffraktometrie vollständig aufgeklärt; jede kristallisiert in einem neuen Strukturtyp. Die ternären Strukturen sind eng mit der Struktur von $NiSi_2$ (CaF_2-Strukturtyp) verwandt; besonders τ_2 stellt anschaulich den Einbau von Au-Atome in die $NiSi_2$-Struktur dar. Die Phase τ_1 bildet sich bei 631℃ in einer peritektischen Reaktion, τ_2 wird bei 608℃ in einer peritektoiden Reaktion geb ildet.
Ein vollständiges Scheil-Diagramm, eine Liquidus-Projektion and vier vertikale Schnitte (10at% Au; 15, 30, 60 at% Ni) wurden erstellt. Die Interpretation der Phasenreaktionen ist bis 700℃ aufgrund der isother men Schnitte gesichert. Für Reaktionen bei höheren Temperaturen wurde ein Vorschlag erstellt, der allerdings teilweise spekulativen Charakter hat.
Abschließend wurden Benetzungsversuche durchgeführt, um die Benetzung der eutektischen Au-Si-Mischung auf einer Nickel-Platte zu untersuchen. Dabei konnte jedoch keine Benetzung beobachtet werden; dies entspricht ähnlichen Versuchen mit einer Kupferplatte.

Weitere Experimente sind notwendig, um das vorgeschlagene Reaktionsschema bei höheren Temperaturen zu bestätigen. Dafür sind Untersuchungen von isothermen Schnitten bei Temperaturen über 700℃ (z.B. 900℃) empfehlenswert. Vor allem im Si-armen Bereich sind mehr Daten notwendig, um das Reaktionsschema aufzuklären.

8 References

[1] http://www1.asminternational.org/asmenterprise/apd/help/intro.aspx, 2014.
[2] P. Villars, Handbook of ternary alloy phase diagrams
P. Villars, A. Prince, and H. Okamoto eds., ASM International, Metals Park, OH, 1995.
[3] K.C.P. B. Ressel, S. Heun, Y. Homma, J. Appl. Phys., 93 (2003) 3886-3892.
[4] S.H.L. K.N. Tu, J. Appl. Phys., 48 (1977) 420-421.
[5] V.Z. Y.V. Naidich, N. Krasovskaya, Mater. Sci. Eng., 245 (1993) 293-299.
[6] S.K. B. Drevet, N. Eustathopoulos, Acta Metallurgica et Materialia, 41 (1993) 3119-3126.
[7] M.L.M. G.W. Liu, F. Valenza, A. Passerone, Ceramics International, 36 (2010) 1177-1188.
[8] K.S.K. G.S. Chung, F. Yakuphanoglu, Journal of Alloys and Compounds, 507 (2010) 508-512.
[9] Ö.G. G. Güler, Ö.F. Bakkaloglu, A. Türüt, Physica B: Condensed Matter, 2008 (2008) 2211-2214.
[10] Y.G. C. Nuhoglu, Vacuum, 84 (2010) 812-816.
[11] W. Klement, Jr., R.H. Willens, P. Duwez, Noncrystalline structure in solidified gold-silicon alloys, Nature (London, United Kingdom), 187 (1960) 869-870.
[12] J. Schroers, B. Lohwongwatana, W.L. Johnson, A. Peker, Precious bulk metallic glasses for jewelry applications, Materials Science & Engineering, A: Structural Materials: Properties, Microstructure and Processing, 449-451 (2007) 235-238.
[13] J. Schroers, B. Lohwongwatana, W.L. Johnson, A. Peker, Gold based bulk metallic glass, Applied Physics Letters, 87 (2005) 0619121-0619123.
[14] H. Ipser, Phasendiagramme, lecture, 2012.
[15] K. Richter, Experimental methods for phase diagram determination, lecture, 2013.
[16] H. Schumann, Metallographie, 8., verb. Aufl. ed., VEB Dt. Verl. f. Grundstoffindustrie, Leipzig, 1974.
[17] F.N. Rhines, Phase diagrams in metallurgy, McGraw-Hill, New York, NY u.a., 1956.
[18] http://www.me.rochester.edu/courses/ME280/, 2014.
[19] http://www.chm.bris.ac.uk/~chdms/Teaching/Chemical_Interactions/page_25.htm, 2014.
[20] http://zeiss-campus.magnet.fsu.edu/articles/basics/reflected.html, 2014.
[21] http://www.olympusmicro.com/primer/techniques/polarized/polarizedhome.html, 2014.
[22] http://www.porous-35.com/appendix-2.html, 2014.
[23] J.I. Goldstein, Scanning electron microscopy and x-ray microanalysis, 2. ed., Plenum Press, New York, NY u.a., 1992.
[24] B.D. Cullity, S.R. Stock, Elements of X-ray diffraction, 3. , 4. print. ed., Prentice Hall, Upper Saddle River, NJ u.a., 2001.
[25] R. Jenkins, Introduction to X-ray powder diffractometry, Wiley, New York, 1996.
[26] W. Massa, Crystal structure determination, 2. ed., Springer, Berlin u.a., 2004.
[27] http://encyclopedia2.thefreedictionary.com/x-ray+diffraction, 2014.
[28] http://serc.carleton.edu/research_education/geochemsheets/techniques/SXD.html, 2014.

References

[29] H. Flandorfer, Synthese und Thermodynamische Charakterisierung, lecture, 2012.
[30] http://www.hitachi-hitec-science.com/en/products/thermal/tec_descriptions/dta.html, 2014.
[31] http://ruby.chemie.uni-freiburg.de/Vorlesung/fk_chemie_2_3.html, 2014.
[32] H. Okamoto, T.B. Massalski, The Au-Si system, Bulletin of Alloy Phase Diagrams, 4 (1983) 190.
[33] P. Villars, L.D. Calvert, Pearson's handbook of crystallographic data for intermetallic phases
by P. Villars and L. D. Calvert, ASM International, Materials Park, Ohio, 1991.
[34] H. Fujii, S. Tahara, Y. Kato, S. Kohara, M. Itou, Y. Kawakita, S.i. Takeda, Structural properties of liquid Au-Si and Au-Ge alloys with deep eutectic region, Journal of Non-Crystalline Solids, 353 (2007) 2094-2098.
[35] A. Pasturel, E.S. Tasci, M.H.F. Sluiter, N. Jakse, Structural and dynamic evolution in liquid Au-Si eutectic alloy by ab initio molecular dynamics, Physical Review B, 81 (2010) 140202.
[36] T.B. Massalski, Binary alloy phase diagrams, 2. ed., Metals Park, Ohio, 1996.
[37] T.A. Hall, A.A. Johnson, The solidus and liquidus lines in the gold-nickel phase diagram, Journal of the Less-Common Metals, 141 (1988) L19-L22.
[38] P. Nash, A. Nash, The Ni-Si (nickel-silicon) system, Bulletin of Alloy Phase Diagrams, 8 (1987) 6-14.
[39] Y. Du, J.C. Schuster, Experimental investigations and thermodynamic descriptions of the Ni-Si and C-Ni-Si systems, Metallurgical and Materials Transactions A-Physical Metallurgy and Materials Science, 30 (1999) 2409-2418.
[40] K.W. Richter, K. Chandrasekaran, H. Ipser, The Al-Ni-Si phase diagram. Part II: phase equilibria between 33.3 and 66.7 at.% Ni, Intermetallics, 12 (2004) 545-554.
[41] D. Mangelinck, P. Gas, J.M. Gay, B. Pichaud, O. Thomas, Effect of Co, Pt, and Au additions on the stability and epitaxy of NiSi2 films on (111)Si, J. Appl. Phys., 84 (1998) 2583-2590.
[42] A. Prince, G.V. Raynor, D.S. Evans, Au-Ni-Si, in: Phase Diagrams of Ternary Gold Alloys, The Institute of Metals, London, 1990, pp. 330-331.
[43] G. Reisinger, Untersuchungen im Phasendiagramm Au-Ni-Si, University of Vienna, 2014.
[44] B.G. Hyde, S. Andersson, Inorganic crystal structures, Wiley, New York u.a., 1989.
[45] NIST, F.I.Z. Karlsruhe, Inorganic Crystal Structure Database, 2014.
[46] A. Blazevic, Phase equlibria and structural investigations in the ternary system Au-Cu-Si, University of Gothenburg, 2013.

9 Appendices

9.1 List of figures

Figure 1: Binary and ternary phase diagram plots (schematic) [1, 18] 6
Figure 2: Projection of vertical sections, isothermal section and schematic liquidus surface view [1].... 7
Figure 3: Binary phase diagram, lever rule [19] 8
Figure 4: Ternary invariant reaction: ternary eutectic [15]..... 9
Figure 5: Ternary invariant reaction: ternary peritectic [15]..... 9
Figure 6: Ternary invariant reaction: ternary transition [15] 10
Figure 7: Schematic view of light optical microscope [20]..... 10
Figure 8: Effects after interaction of electron beam with sample [22] 12
Figure 9: Setup of XRD with Bragg-Brentano pseudo focusing circle [27] 13
Figure 10: Setup of single crystal XRD [28] 16
Figure 11: Principal setup of differential thermal analysis [30]..... 17
Figure 12: Binary phase diagram and reactions in DTA [31] 18
Figure 13: Binary phase diagram Au-Si [36] 20
Figure 14: Binary phase diagram Au-Ni [36] 21
Figure 15: Binary phase diagram Ni-Si with revised grey field [36]..... 22
Figure 16: Revised section of Ni-Si-phase diagram by Richter [40] 23
Figure 17: Sample preparation before annealing..... 26
Figure 18: Sample preparation after annealing..... 26
Figure 19: Prepared samples located in ternary phase diagram 27
Figure 20: Zeiss Axiotech 100 microscope 29
Figure 21: Zeiss Supra 55VP SEM/EPMA 30
Figure 22: Powder-XRD BRUKER D8..... 31
Figure 23: Single crystal-XRD Bruker Nonius KappaCCD FR590..... 31
Figure 24: DTA-instrument Setaram Setsys Evolution TGA & DTA 2400 32
Figure 25: temperature program for DTA-measurement..... 32
Figure 26: Sample A16 – left: SEM-image, right: LOM-image..... 33
Figure 27: Isothermal section at 320℃; dashed line s are not confirmed by experiments..... 34
Figure 28: Sample B4 – left: SEM-image, right: LOM-image..... 36
Figure 29: Isothermal section at 500℃; dashed line s are not confirmed by experiments..... 38
Figure 30: XRD-pattern of B3; green: experiment; red: refinement; grey: difference 39
Figure 31: XRD-pattern of A8 with metastable $Au_{17}Si_3$; blue: experiment; red: refinement; grey: difference..... 40
Figure 32: XRD-pattern of B3 with peaks phase of A8; blue: experiment; red: refinement; grey: difference; dashed blue: peaks phase of metastable $Au_{17}Si_3$ 40
Figure 33: Sample D9 – left: SEM-image, right: LOM-image..... 41
Figure 34: Isothermal section at 700℃; dashed line s are not confirmed by experiments..... 43
Figure 35: Unit cell of τ_1..... 44
Figure 36: Sample B7- left: SEM-image, right: LOM-image..... 45
Figure 37: DTA-curve (first heating) of sample A5 = blue curve; red circle: exothermic effect caused by the formation of the ternary phase 45
Figure 38: Different phase fields of samples A5, A12, A17..... 46
Figure 39: Pre-treatment of samples A5, A12, A17 46
Figure 40: XRD-pattern of B7; blue: experiment; red: refinement; pink: calculated τ_1-pattern, missing lines correspond to $Au_{17}Si_3$ (metastable) 48
Figure 41: Atom-coordination of $NiSi_2$ – left: Nickel; right: Silicon..... 48
Figure 42: Unit cell of τ_2..... 50
Figure 43: SEM-image of sample B5 50
Figure 44: X-ray-diffractogram of B5; blue: experiment; red: refinement; green: calculated τ_2-pattern 52
Figure 45: Comparison of τ_2 & $NiSi_2$ (polyhedral view) 53
Figure 46: Scheil diagram (reaction scheme) of Au-Ni-Si system..... 56
Figure 47: Isopleth of Au-Ni-Si system at 10at% gold..... 58
Figure 48: Isopleth of Au-Ni-Si system at 15at% nickel 59
Figure 49: Isopleth of Au-Ni-Si system at 30at% nickel 60
Figure 50: Isopleth of Au-Ni-Si system at 60at% nickel 61
Figure 51: Liquidus surface projection of Au-Ni-Si system 62

Appendices

Figure 52: Positioning of the Au-Si-piece on the nickel plate – left: without ballast; right: two nickel plates act as a ballast 64
Figure 53: Piece of Au-Si on nickel plate – left: before heating; right: after heating 64
Figure 54: Wetting experiment with two nickel plates as ballast – left: before heating; right: after heating (Au-Si piece shifted away) 65
Figure 55: Temperature program for wetting experiment 65

9.2 List of tables

Table 1: Phases of binary system Au-Si [32] 20
Table 2: Reactions of binary system Au-Si [32] 20
Table 3: Phases of binary system Au-Ni [37] 21
Table 4: Reactions of binary system Au-Ni [37] 21
Table 5: Phases of binary system Ni-Si [38, 40] 23
Table 6: Reactions of binary system Ni-Si [38, 40] 23
Table 7: Overview of all prepared samples 28
Table 8: Experimental data of XRD- & EPMA-analysis at 320℃ 35
Table 9: Experimental data of XRD- & EPMA-analysis at 500℃ 37
Table 10: Experimental data of XRD- & EPMA-analysis at 700℃ 41
Table 11: Symmetry and unit cell parameters of τ_1 47
Table 12: Atom positions of τ_1 47
Table 13: Atom positions of τ_1 – Au on the 4-fold-position 47
Table 14: Comparison of τ_1 & $NiSi_2$ (atom-coordination) 49
Table 15: Symmetry and unit cell parameters of τ_2 51
Table 16: Atom positions of τ_2 51
Table 17: Comparison of τ_2 & $NiSi_2$ (atom-coordination) 53

9.3 Curriculum Vitae

Name: Matthias Stacher
Citizenship: Austria

Education and Work Experience

Since Oct. 2012 Study of chemistry at the University of Vienna (Master)

- since Oct. 2013 Master thesis „Investigation of the ternary phase diagram of Au-Ni-Si“ at the Department for Inorganic Chemistry (Materials Chemistry)

2009 - 2012 Study of chemistry at the University of Vienna (Bachelor)

- Bachelor thesis „Electrochemical investigations of 3-nitro-phthalic acid“ at the Department for Physical Chemistry

2005 - 2009 Robert BOSCH AG, Vienna

- Hardware-R&D (Control units for diesel engines)

2002 – 2005 IVM – Engineering, Vienna

- Hardware-R&D (Control units for diesel engines), at Robert BOSCH AG, Vienna

2001 – 2002 Civilian service (Landesklinikum Mistelbach)

1995 – 2000 Higher Technical Institute for Control engineering (Hollabrunn)

1991 – 1995 secondary school (Ernstbrunn)